Lawrence Berkeley National Laboratory

Title
Hydrological control of rock carbon fluxes from shale weathering

Permalink

Authors
Wan, Jiamin
Tokunaga, Tetsu K
Beutler, Curtis A
et al.

Publication Date

DOI

Hydrological control of rock carbon fluxes from shale weathering

Check for updates

Jiamin Wan [1] ✉, Tetsu K. Tokunaga [1] ✉, Curtis A. Beutler[2], Alexander W. Newman[2], Wenming Dong [1], Markus Bill [1], Wendy S. Brown[2], Amanda N. Henderson[2], Anh Phuong Tran[3] & Kenneth H. Williams [1,2]
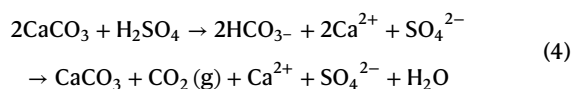
Shale bedrocks hold Earth's largest carbon inventory. Although water is recognized for cycling elements through terrestrial environments, understanding how hydrology controls ancient rock carbon (C_{rock}) release is limited. Here we measured depth- and season-dependent subsurface water fluxes and pore-water and pore-gas geochemistry (including radiocarbon) over five vastly different water years along a hillslope. The data reveal that the maximum depth of annual water table oscillations determines the weathering depth. Seasonally varying subsurface water fluxes determine the export forms and rates of weathered C_{rock}. Eighty percent of released C_{rock} is emitted as CO_2 to the atmosphere primarily during warmer and lower water table seasons and 20% of released C_{rock} as bicarbonate exports mostly during months of snowmelt to the hydrosphere. Thus, the rates and forms of C_{rock} weathering and export are clearly controlled by climate via hydrologic regulation of oxygen availability and subsurface flow. The approaches developed here can be applied to other environments.

Appreciation for water's worldwide importance is longstanding and reflected in Leonardo da Vinci's proclamation that 'Water is the driving force of all nature'. Water is indeed essential in the physical and chemical weathering of rock, releasing and transporting elements including carbon back into the environment[1–4], yet a hydrologically realistic accounting of subsurface flow is required for understanding this part of the rock cycle. Shales covers 25% of Earth's continental surface area[5] and possess large inventories of rock-contained organic carbon (OC_{rock}) and inorganic carbon (IC_{rock}) as carbonate, and sulfide minerals[1,6]. Chemical weathering of shale bedrock can release CO_2 back to the atmosphere by the oxidative weathering of sulfide minerals and rock organic matter, whereas chemical weathering of silicate minerals captures CO_2[1,7–9]. The dynamics of subsurface water control shale weathering through regulating oxygen availability, which in turn control pyrite and OC_{rock} oxidation and through transport of dissolved weathering products. Above the water table, microbial respiration transforms OC_{rock} to CO_2[10,11] (equation (1)), and oxidative dissolution of pyrite commonly present in shales generates sulfuric acid (equation (2)), which in turn dissolves carbonate minerals and

releases CO_2 to atmosphere (equations (3) and (4)). Depending on the pore-water acidity, the transformation of carbonate to CO_2 can take two steps (equation (4)). These are the most kinetically favourable reactions for shale weathering, although carbonic acid (H_2CO_3) from CO_2 dissolution also drives carbonate dissolution and silicate weathering[1].

$$(OC)_{rock} + O_2 \rightarrow CO_2\,(g) + H_2O \tag{1}$$

$$4FeS_2 + 15O_2 + 14H_2O \rightarrow 4Fe(OH)_3 + 8H_2SO_4 \tag{2}$$

$$CaCO_3 + H_2SO_4 \rightarrow CO_2\,(g) + Ca^{2+} + SO_4^{2-} + H_2O \tag{3}$$

and/or

$$2CaCO_3 + H_2SO_4 \rightarrow 2HCO_{3-} + 2Ca^{2+} + SO_4^{2-}$$
$$\rightarrow CaCO_3 + CO_2\,(g) + Ca^{2+} + SO_4^{2-} + H_2O \tag{4}$$
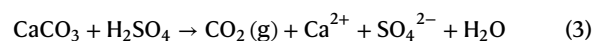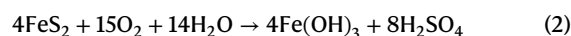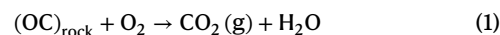
[1]Earth and Environment Sciences Area, Lawrence Berkeley National Laboratory, Berkeley, CA, USA. [2]Rocky Mountain Biological Laboratory, Crested Butte, CO, USA. [3]Water Resources Institute, Hanoi, Vietnam. ✉e-mail: jwan@lbl.gov; tktokunaga@lbl.gov
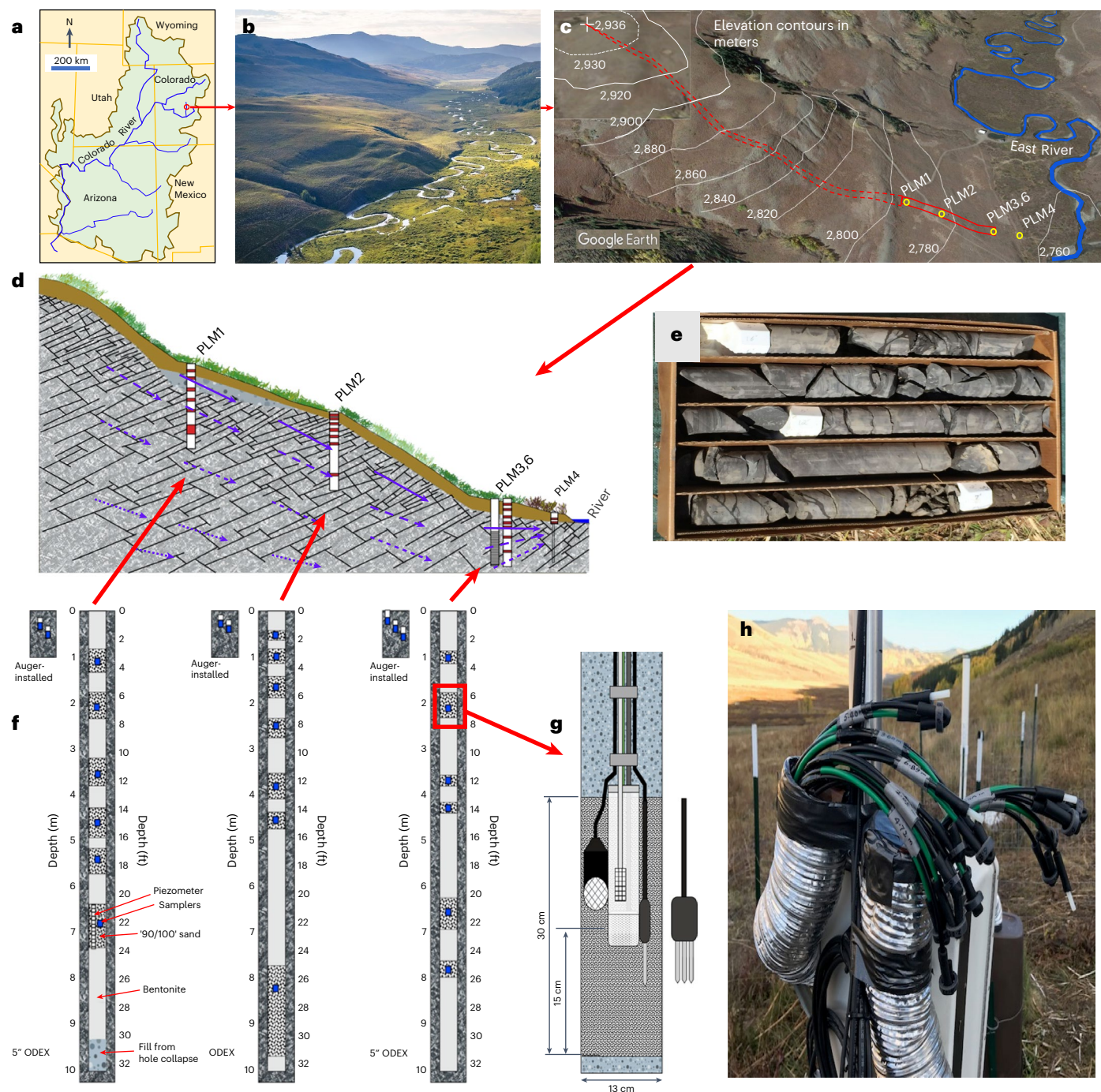
Fig. 1 | The study site and borehole instrumentation. a, Map of the Colorado River Basin, showing location of the East River watershed. **b**, Upper East River watershed, view towards south. **c**, Hillslope flow transect topography from its peak at 2,936 m elevation down to the East River at 2,755 m. **d**, Borehole locations of PLM1, 2, 3, 4 and 6, with PLM3 and 6 located at the toe slope. PLM 4 is in the floodplain. PLM 6 is 5 m away from PLM 3 at the same elevation. PLM 2 is located 2 m higher in elevation relative to the average hillslope profile. **e**, Mancos Shale core samples collected during drilling. **f**,**g**, Three of the five boreholes were instrumented with pore-water and pore-gas samplers, and sensors for measuring pressure, matric potential, moisture content and temperature. ODEX (Overburden Drilling EXcentric) is a type of drilling used to access and sample strata composed of rock or boulders. **h**, Elevated outlets for collecting pore-water and pore-gas samplers even under snow cover. These instruments provided five years of time- and depth-dependent hydrologic and geochemistry measurements. Map in **a** from the US Bureau of Reclamation (http://www.usbr.gov/ColoradoRiverBasin/). Credit: **b**, Jeremy Snyder; **c**, Google Earth.

Current models for C_{rock} weathering are largely based on rates of mountain uplift and erosion of exhumed rocks from the land surface of vast river systems over geological timescale[1,4,12,13]. Measurements of bedrock-sourced dissolved C, S, trace elements and particulate C in rivers have quantified C_{rock} exports from watersheds[4,8,14–19], and insights into bedrock weathering at the hillslope to watershed scales is developing[20–32]. However, the subsurface hydrologic link between weathering C_{rock} profiles and C_{rock} exports in rivers has remained obscure. The unique contributions of the present study come from obtaining depth- and time-resolved subsurface measurements needed to explicitly connect weathering profiles to their watershed solute exports, with particular attention on determining C_{rock} fluxes. The data obtained over multiple continuous years having large differences in precipitation may also provide insights into impacts of climate change on weathering.

Building on these past studies, the dynamics of C_{rock} release can be further understood by combining spatially and temporally resolved subsurface measurements of C (including C_{rock}) along a hillslope with a recent investigation that quantified subsurface flow at the site[33]. Elucidating the dependence of C_{rock} weathering on water table dynamics and subsurface flow will enable linking measurements of weathering processes to predictions of watershed-scale C_{rock} discharges into surface waters and emissions to the atmosphere.

This Article presents the outcomes of a five-year field and laboratory endeavour to understand how subsurface water dynamics control weathering and release of C_{rock}. We determined depth- and season-resolved water fluxes, coupled with season- and depth-resolved measurements of pore-water and pore-gas geochemistry, including radiocarbon dating, to obtain fluxes of C to the hydrosphere and atmosphere. The study was conducted in the Upper Colorado River Basin, East River watershed, along a lower montane hillslope underlain by Mancos Shale (Fig. 1a–e). On a hillslope-to-floodplain flow transect (Fig. 1b–d), we drilled five boreholes 10 m deep into the bedrock, collecting rock cuttings and core samples (Fig. 1e). Three of the boreholes were instrumented at different depths with sensors for measuring hydraulic potentials, moisture content and temperature (Fig. 1f,g) and samplers for collecting pore waters and pore gas (Fig. 1h) over five years. Knowledge of weathering zone depths is crucial for quantifying weathering rates and C fluxes. In this Article we define the depth interval where weathering reactions are most active[22] as the 'weathering zone' (WZ), define its lower boundary where geochemical conditions support weathering as the 'weathering front' (WF) for specific rock components and the zone below the WF as the 'fractured bedrock' (FBR).

Water table dynamics drive subsurface flow

The very high permeability of the hillslope soil accommodates infiltration from melting snowpack, prevents overland flow and further supports the importance of subsurface flow on rock weathering[22,33]. Water mass balance was used to constrain recharge that drives groundwater flow and reflects the competition between precipitation and evapotranspiration (ET) (Fig. 2a). Because ET from late spring through fall in this environment is high enough to prevent deep infiltration from rainfall, recharge of groundwater only occurs during spring snowmelt and is incompletely drained from the WZ in high snowmelt years. Dissolved products of weathering are removed in discharging waters, necessitating quantitative information on seasonal- and depth-dependent flow for calculating rates of bedrock weathering and solute transport. We calculated water mass balances over five years with effective annual precipitation P_e values (Methods) that optimize for interannual changes in subsurface water storage through carrying over precipitation exceeding a threshold high snowpack water mass into the following year. Thus, on a water year (WY) basis, annual subsurface flow is equated with P_e – ET (ref. 33).

The water table rises sharply during spring snowmelt, extending (in high snow years) into the soil, and declines to its lowest depths just before the following year's snowmelt (Fig. 2b). Gravity-driven subsurface flow within the hillslope depends on the elevation of the water table, hydraulic properties of each zone and the nearly constant water table slope, which remains parallel to the soil surface. The transmissivity (T) within a given zone is its hydraulic conductivity (K) times its saturated thickness, and the transmissivity feedback model[34] provides a suitable representation for subsurface flow in many hillslopes such as ours where values of K increase towards the soil surface. The values of K for the soil and WZ and the value of T for the FBR were optimized so that calculated fluxes best matched P_e – ET over the course of five years (Methods). Daily groundwater flow rates through each zone (Fig. 2c) were calculated based on the transmissivity feedback model and continuous water table elevation measurements (Fig. 2b). Flow through the FBR is relatively steady because it remains fully saturated and the hydraulic gradient exhibits only minor fluctuations. Flow through the WZ oscillates annually in response to the continuously varying

water table depth that drives variations in its saturated thickness. The nonlinear dependence of flow on water table depth reflects the much higher K values in the WZ and soil relative to the FBR. When snowmelt is sufficient to raise the water table above the WZ, rapid downslope flow of shallow groundwater occurs along the soil. Although such periods with high water table are short (absent in low snow years), they enable very high flow (up to 72% of the annual recharge) because of the high K_{soil}. Annual partitioning of groundwater flow between the two months of maximum snowmelt and ten 'baseflow' months with lower discharge is shown in Supplementary Fig. 1a. These measurements of dynamic water table depths and stratified water fluxes make quantification of weathering rates possible.

Quantifying C_{rock} weathering release

Three approaches were used to estimate rates of IC_{rock} weathering: sulfate discharge, base cation discharge and eroded IC_{rock} profile reconstruction (Methods). The lowest estimate assumes that IC_{rock} is only released in equimolar amounts with sulfate discharged upon pyrite oxidation. Time trends for sulfate concentrations measured from pore-water samples were plotted for the three depth zones (Fig. 3a), which were then multiplied by their corresponding subsurface water fluxes (Fig. 2c) to obtain rates of subsurface sulfate export within each zone and from the total subsurface (Fig. 3b). Export of sulfate and the other rock components in groundwater drives reactions (equations (1)–(4)) through removal of weathering products. Over the course of five years, sulfate was removed at a rate of 394 ± 267 kmol km^{-2} yr^{-1} with the 'plus-minus' values indicating standard deviations among the five annual rates. The partitioning of exports for sulfate and other solutes between months of peak flow versus baseflow are shown in Supplementary Fig. 1, showing significant dilution by snowmelt during high snowpack years and increased concentrations during baseflow. It should be noted that snowmelt includes solutes from the soil and WZ released above the water table during the preceding baseflow interval. Whereas most of the acidity from pyrite dissolution drives IC_{rock} dissolution, given that the IC_{rock}:pyrite ratio of 4.26 mol mol^{-1} in the unweathered bedrock (Extended Data Table 1) only slightly exceeds 4.0[27], a small fraction of acid from pyrite oxidation could contribute to silicate dissolution and C sequestration.

The second approach assumed that IC_{rock} releases occur in proportion to its bedrock concentration relative to bedrock base cations (BC) concentration, given that BC export rates are often used to quantify weathering rates[35,36]. Multiplying zone-specific pore water BC concentrations (Fig. 3c) by their corresponding subsurface water fluxes (Fig. 2c) yielded rates of BC exports within each zone and for the total subsurface (Fig. 3d). Over the course of five years, a BC export of $1,420 \pm 530$ kmol$_c$ km^{-2} yr^{-1} was obtained, similar to rates reported for other sedimentary watersheds[36,37]. On the basis of our measured IC_{rock}:BC_{rock} ratio of 0.32 mol mol$_c^{-1}$, the BC-based estimate for IC_{rock} release is 447 ± 170 kmol C km^{-2} yr^{-1}. This estimate for IC_{rock} release is 13% greater than that obtained based on sulfate export, consistent with a small contribution from dissolution by carbonic acid.

Reconstruction of the eroded IC_{rock} depth involved estimating the depleted sulfur solid phase inventory in the present profile (the yellow shaded area in Fig. 3e) and assuming the measured sulfate release rate of 394 kmol km^{-2} yr^{-1} (Fig. 3b) represents the average rate since recession of the Pinedale Glacier 16 thousand years ago (ka) (ref. 38). The total S removed over this time indicates that about 0.82 m of the post-glacial regolith has eroded away. It is worth noting that the estimated 0.82 m of eroded regolith is equivalent to an erosion rate of 130 t km^{-2} yr^{-1}, within the 42–420 t km^{-2} yr^{-1} range reported for slopes within the Rocky Mountains[39,40]. Adding the eroded thickness on the top of the current IC_{rock} profiles (Fig. 3f) yields an IC_{rock} release rate of 434 ± 41 kmol C km^{-2} yr^{-1} ($\pm$ reflects uncertainty in timing of glacier retreat), remarkably similar to the rates obtained with the other two methods (Fig. 3, inserted table). It should be noted that the depth for
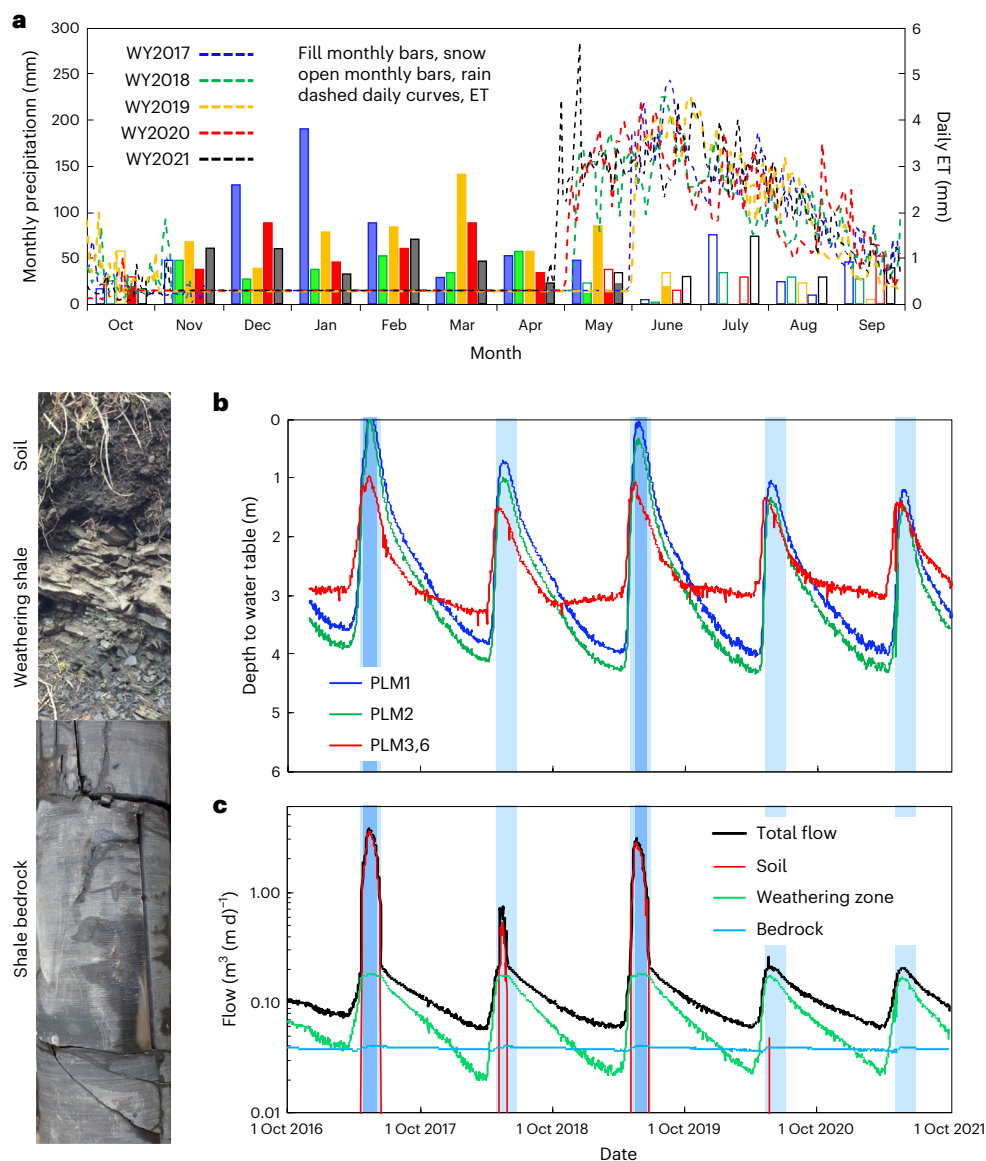
Fig. 2 | Snowmelt drives annual water table oscillations and stratified subsurface water fluxes. The mean annual precipitation is about 600 mm with about 70% as snow. The ground is generally snow covered from November through early May. **a**, Precipitation and ET trends in WY2017–WY2021. Precipitation occurs primarily as snow (filled bars) from November through April and rainfall from May through October (unfilled bars). Calculated ET trends include low rates from snowpack sublimation, followed by high rates of ET losses from late spring into summer. Recharge of groundwater only occurs during spring snowmelt. **b**, Annually oscillating water table depths at the three monitoring locations all show responses to spring snowmelt. **c**, Time-dependent subsurface flow within different depth zones and the total water flux. The light blue background indicates two-month intervals with shallowest water table and highest subsurface flow. The darker blue background indicates intervals when snowmelt was sufficiently high to drive the water table into the soil zone.

the IC_{rock} WF is unclear in the solid phase profiles because of heterogeneous concentrations in unweathered rock and unknown contribution from precipitation of modern carbonates, yet coincides with that of pyrite based on minima in pore water ^{14}C profiles shown later.

An OC_{rock} release rate of 392 ± 37 kmol C km^{-2} yr^{-1} results from similarly adding the eroded thickness on the top of the measured OC_{rock} depletion profile (Fig. 3g). Because higher metamorphic grade or physical protection leaves a fraction of OC_{rock} strongly resistant to oxidation[17,41,42], neither S nor BC exports were used to estimate OC_{rock} oxidation. Whereas oxygen supply from water table lowering was the prerequisite for initiating weathering of pyrite, IC_{rock} and OC_{rock}, differences in their initial concentrations and kinetics resulted in differences in their weathering profiles (Fig. 3e–g). Despite the overall slower oxidation rate of OC_{rock} relative to pyrite, pore-water depletion of ^{14}C in dissolved organic carbon (DOC) profiles shown later support a

WF depth for the more labile fraction of OC_{rock} that coincides with the WFs for pyrite and IC_{rock}.

Another metric for weathering at this East River hillslope was obtained from quantification of Si exports in pore waters, following the procedure described for BC exports. The measured annual Si discharge rates of 16 to 69 kmol km^{-2} yr^{-1} (Supplementary Fig. 1h) are consistent with fluxes from other shale watersheds with similar precipitation and run-off reported by Shaughnessy and Brantley[43].

Quantifying effluxes of DIC, DOC and CO₂

Here exports of total C in porewaters and as CO_2 are quantified, providing the context for C_{rock} releases into porewaters and gas presented in the next section. Time trends in pore-water dissolved inorganic carbon (DIC) concentrations within the three zones are shown in Fig. 4a. DIC concentrations are highest in the WZ and FBR, reflecting weathering
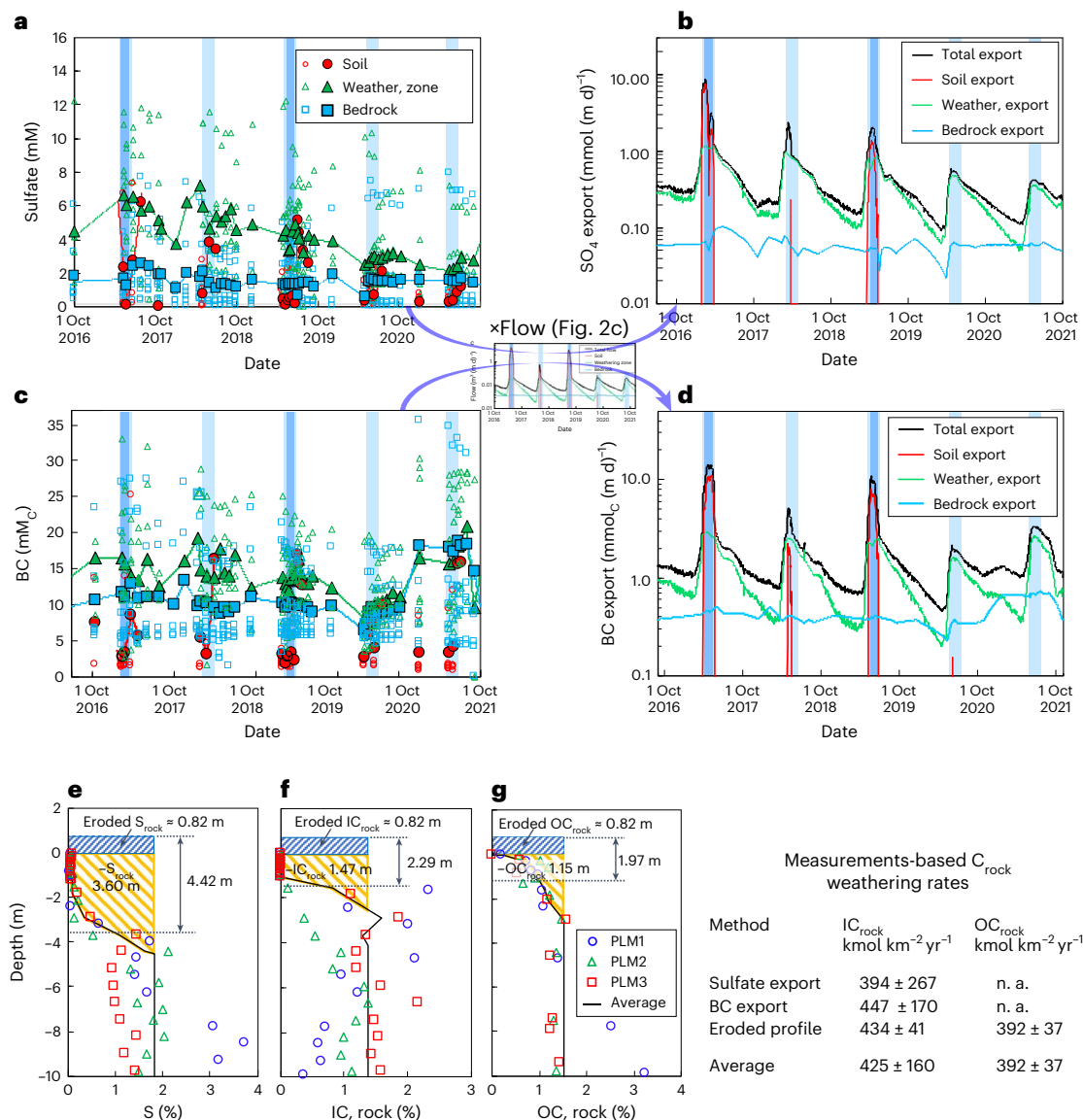
Fig. 3 | Quantifying C_{rock} release rates using three different approaches. **a**, Pore-water sulfate concentrations within each depth zone. Open symbols represent single samples, and filled symbols are averages of at least three samples collected on the same day. **b**, Multiplying the concentration trends from each zone in **a** by their corresponding Darcy water fluxes (Fig. 2c), yielded the trends in daily SO_4 discharge rates from each zone and from the total subsurface. **c**, Pore-water BC concentrations within each depth zone. **d**, Multiplying the BC trends from each zone in **c** by their corresponding Darcy water fluxes (Fig. 2c), yielded the trends in daily BC discharge rates from each zone and from the total subsurface. Note that the highest release rates occur during the two-month periods of snowmelt-driven flow (highlighted with light blue background), especially when the water table rises into the soil (the darker blue background),

and demonstrate strong seasonality of solute export rates (Extended Data Table 3). Variability in annual recharge is largely responsible for the high standard deviations for release rates. The IC_{rock} weathering rates based on these two approaches are presented in the inserted table. **e**, Solid phase sulfur depth profiles from X-ray fluorescence and X-ray diffraction measurements. The yellow shaded area denotes sulfur depletion from weathering. The estimated erosion-removed thickness of 0.82 m was calculated by assuming that sulfur was steadily discharged at the measured average rate (394 kmol km^{-2} yr^{-1}) since recession of the Pinedale glacier about 16 ka ago. **f**, Measured total IC_{rock} profiles, with losses from weathering and erosion. **g**, Measured total OC_{rock} profiles, with losses from weathering and erosion. NA, not applicable.

reactions and elevated partial pressure of CO_2 (P_{CO_2}) with depth and lowest in soil due to the depletion of carbonate minerals and low P_{CO_2}. Multiplying the interpolated daily DIC concentrations within each zone by their respective Darcy fluxes (Fig. 2c) yields rates of DIC discharge (Fig. 4b) and a total DIC export rate of 644 ± 307 kmol km^{-2} yr^{-1}.

Trends for DOC (Fig. 4c) show that the highest concentrations occur in soil, where modern organic carbon enters the subsurface (next section). Export rates for DOC (Fig. 4d) were obtained by multiplying the interpolated daily concentrations within each zone by their corresponding flow rates (Fig. 2c), resulting in a DOC export rate over five years of 98 ± 89 kmol km^{-2} yr^{-1}.

Diffusive losses of CO_2 were calculated (Methods) based on seasonal changes in soil water content (Fig. 4e) and temperature T (Fig. 4f) that cause annual variations in the effective diffusion coefficient for CO_2 at the soil surface (Fig. 4g). The time-dependent CO_2 concentrations from the shallowest soil gas samplers at the three locations (Fig. 4h) remain substantially elevated relative to the atmospheric CO_2 concentration of about 420 ppm, especially under winter snowpack (yellow background), which drives build-up of soil CO_2. These CO_2 concentrations together with other measured parameters (Fig. 4e–i) were used to calculate time-dependent diffusion rates (Fig. 4j). Averaging the rates over the five years yielded a CO_2 efflux of
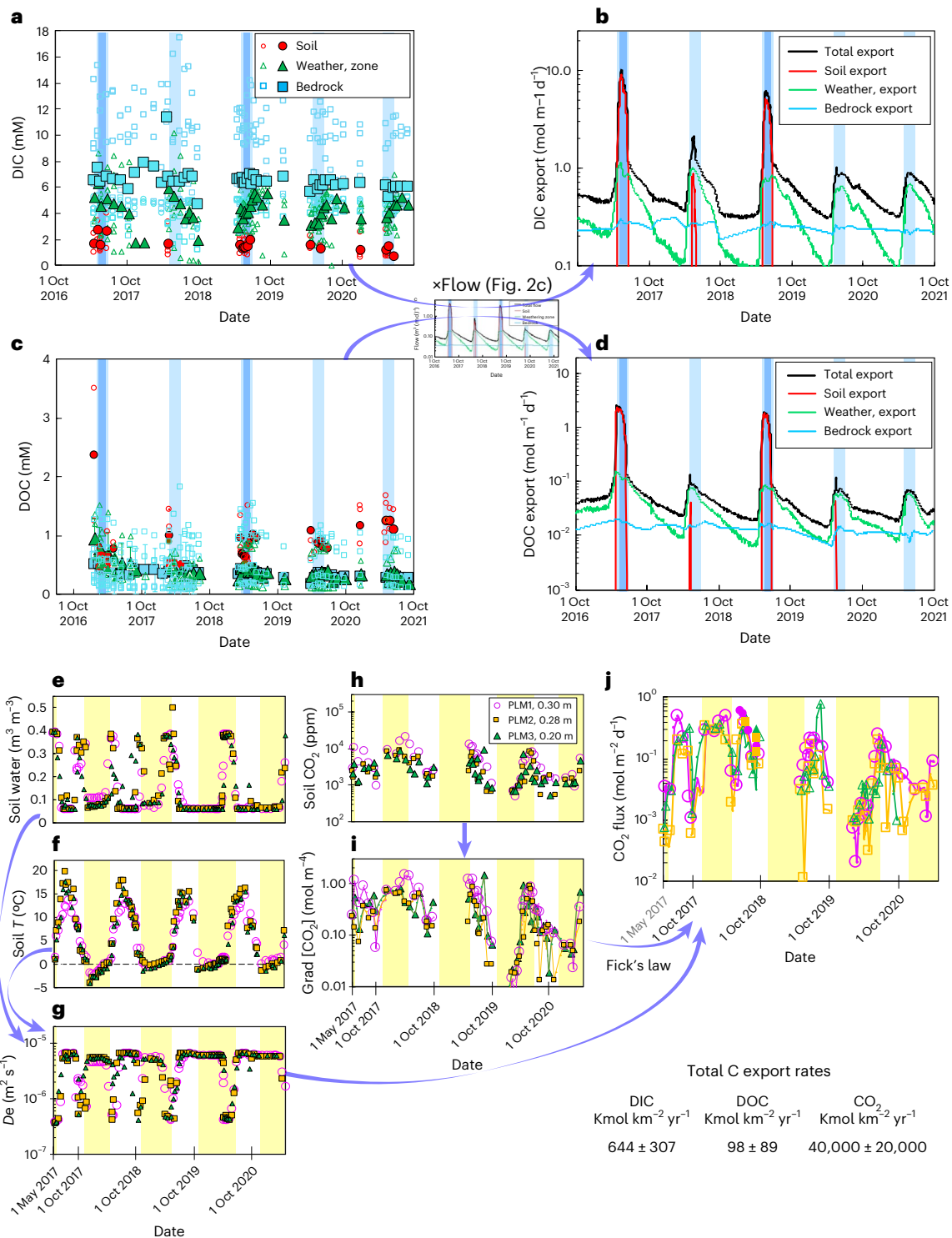
Fig. 4 | Quantifying effluxes of DIC and DOC to hydrosphere and CO₂ to atmosphere. a, Time-dependence of dissolved inorganic carbon (DIC) concentrations within each zone over five years. **b**, Multiplying the DIC concentration trends in each zone by its corresponding Darcy water fluxes from Fig. 2c yielded the daily DIC effluxes for each zone and for the total subsurface. **c**, Dissolved organic carbon (DOC) concentration time trends within each zone. **d**, Multiplying the DOC concentration trends in each zone by its corresponding Darcy water fluxes (Fig. 2c) yielded the daily DOC effluxes for each zone and for the total subsurface. The overall rates of DIC and DOC export from the hillslope are 644 and 98 kmol C km⁻² yr⁻¹, respectively (inserted table). The maximum C export rates occur during the two-month period of snowmelt-driven flow

(highlighted with light blue background), especially when the water table rises into the soil (the darker blue background), and demonstrates the strong seasonality of dissolved C export rates. These annual 'hot moments' account for about 44 ± 21% of annual dissolved C exports. **e–j**, Time-dependence of volumetric water content of surface soil (**e**), surface soil temperature (**f**), effective CO₂ diffusion coefficient (**g**), CO₂ concentrations from the shallowest soil (**h**), CO₂ concentration gradient (**i**) and daily CO₂ emission rates based on Fick's law (**j**). The average CO₂ emission rate 40,000 Kmol C km⁻² yr⁻¹ and its magnitude is supported by flux chamber measurements (filled symbols in **j**). This large CO₂ efflux is predominantly from soil respiration of C_modern. *T*, temperature.
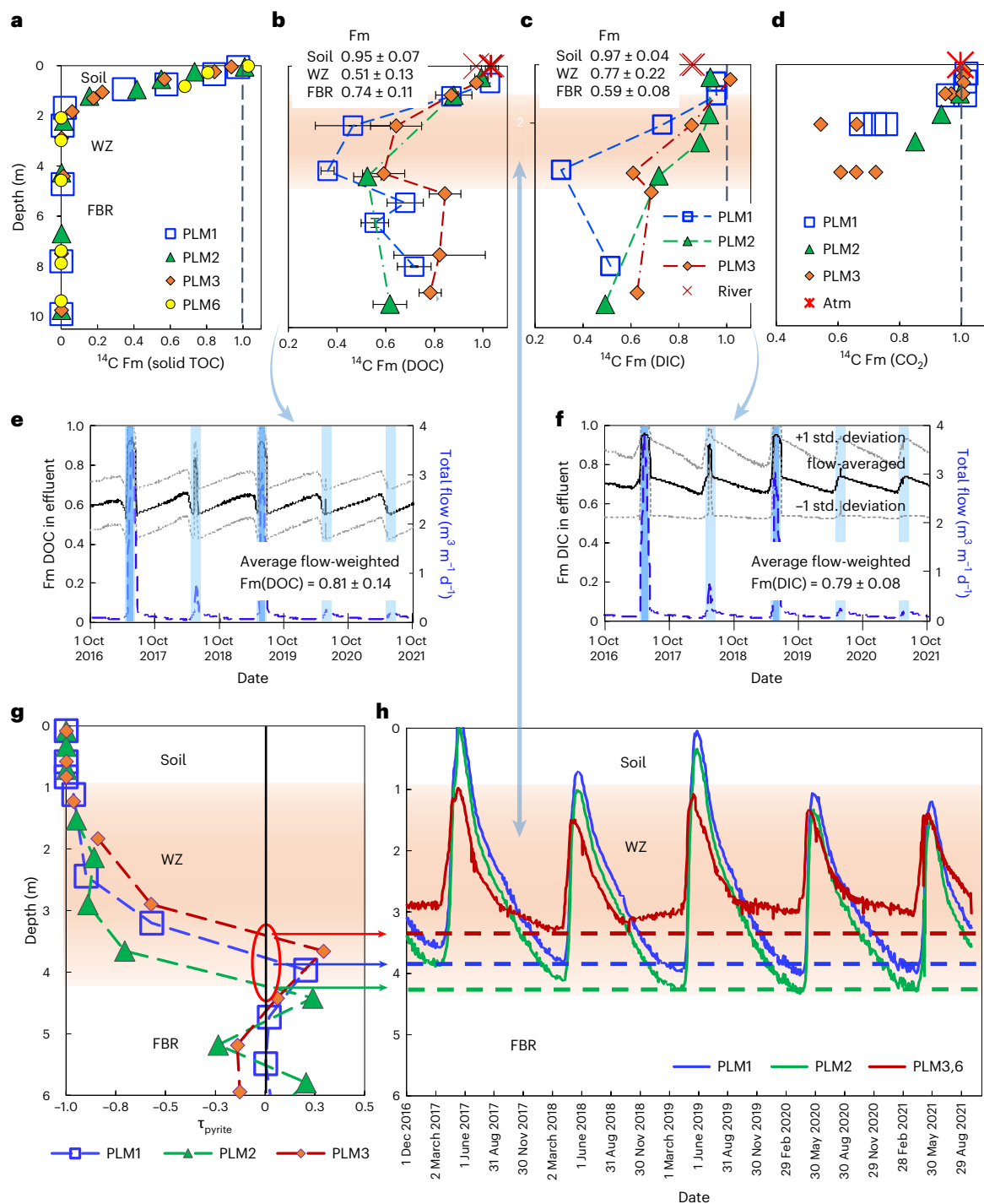
Fig. 5 | Radiocarbon data and applications. a, Measured [14]C Fm of solid phase organic carbon, showing the depths of two Fm end members, at -0 and ≥2 m. **b**, Measured [14]C Fm of DOC in pore water (three sampling dates in 2018–2020) and river. The standard deviations are shown in the error bars. **c**, Measured [14]C Fm of DIC in pore water (sampled in spring 2020) and river. All river water samples were collected in 2018 and 2020, *n* = 3, at the same location. Inserted tables show average [14]C Fm values used in calculating C_{rock}:C_{modern} ratios in effluxes. **d**, Measured [14]C Fm of CO_2 in pore gas. **e,f**, Calculated [14]C Fm in DOC and DIC effluxes, respectively (averages and standard (std.) deviations). **g**, Measured

pyrite concentrations expressed as relative concentration profiles using the τ plot method, which identified the weathering front at the depth τ > →0 for each of the three boreholes. The orangish background is used to denote the range of WZ depths. **h**, The water table minima at each location matches the weathering front depths identified by the pyrite τ profiles. Together with the [14]C Fm of DOC and DIC (**b,c**), these measurements show that the range of water table oscillation defines the weathering zone and the lowest water table depth defines the weathering front.

4,000 ± 2,000 kmol C km^{-2} yr^{-1}, within the range of soil respiration rates reported from similar environments[44,45]. As shown next, this expected large CO_2 efflux is predominantly C_{modern} from soil respiration and is outside the scope of this study.

Radiocarbon data and applications

Radiocarbon (^{14}C) relative concentrations expressed as fraction modern (Fm) were determined in samples of solid OC_{bulk} from soil to bedrock, DOC and DIC in depth-resolved pore waters and pore-gas CO_2
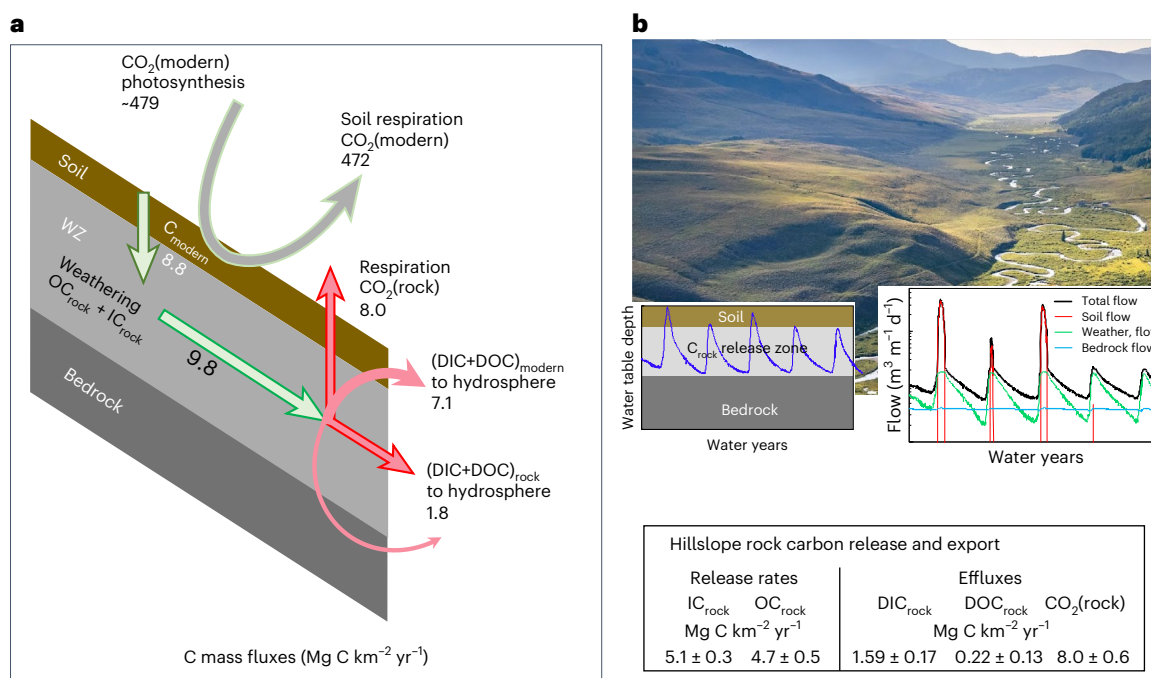
Fig. 6 | Hydrological control on shale weathering and C cycle in mountains. a, Hillslope C mass balance model with emphasis on rock C contributions. The fluxes are also summarized in inserted table. All C fluxes, including the large soil respiration efflux of modern CO_2, are measurements based except for the photosynthetic modern CO_2 influx, which is assumed equal to the total modern C efflux. **b**, The water table depth minima and annual oscillation range determine the weathering front and weathering zone locations and the stratified subsurface water fluxes that control discharges of weathering products. The water table minimum is driven to greater depths (red line) following successive drought years (WY2020 and WY2021) and supplies oxygen to previously saturated, reduced bedrock. Credit: **b**, Jeremy Snyder.

(Methods). For soil with shale as the parent material (shale fragments are abundant in soil), the OC_{bulk} contains OC_{rock} (Fm = 0) and biosphere OC (OC_{bio}) (Fm ≤ 1). The measured Fm_{bulk} from soil to bedrock (Fig. 5a) indicate two end members and their depths: $Fm_{bulk} ≈ 1.0$ at 0–0.05 m and $Fm_{bulk} = 0$ at ≥2.0 m. Whereas ageing of OC_{bio} occurs[46,47], Fm_{bio} values depend on the integrated rates of OC_{bio} formation and degradation. To estimate the Fm_{bio} value above 2.0 m, we applied two approaches[17,48] (Methods), and both support the approximation that $Fm(OC_{bio}) ≈ 1.0$ in this system.

Fm(DOC) and Fm(DIC) values remain distinct in the three subsurface zones despite pore waters undergoing some mixing during flow (Fig. 5b,c). Fm(DOC) = 1.00 (± 0.03) in soil pore waters, showing that the signature from OC_{rock} weathering is overwhelmed by OC_{modern} release in the soil. The Fm(DIC and DOC) values decrease with depth to their minima at about 4 m (the WF), showing C_{rock} weathering occurs primarily in the WZ. Furthermore, these data provide the new insight that OC_{rock} and IC_{rock} share the same WF depth, despite having different weathering rates. In pore-gas profiles (Fig. 5d), high rates of OC_{bio} respiration keep $Fm(CO_2) ≈ 1.0$ within soil, whereas $Fm(CO_2)$ values as low as 0.55 in the WZ demonstrate substantial transformation of C_{rock} to CO_2.

To calculate the C_{rock} portion from the total C in groundwaters discharged from the hillslope, the average Fm(DOC) and Fm(DIC) in each depth zone (Fig. 5b,c inserted tables) were weighted by their zone-specific flow rates (Fig. 2c) to obtain Fm discharge trends (Fig. 5e,f). The average Fm(DOC) = 0.81 ± 0.09 and Fm(DIC) = 0.79 ± 0.13 for waters discharged from the hillslope (± indicate flow-weighted variation based on standard deviations of FM within each zone) and is consistent with hydrologic analyses showing that most of the snowmelt discharges via shallow subsurface flow[33,49]. The broader watershed contains areas with and without shale bedrock[49], resulting in higher Fm(DOC) = 0.94 ± 0.14 and Fm(DIC) = 0.86 ± 0.007 in the river (Fig. 5b,c).

The pore water Fm(DOC) and Fm(DIC) depth profiles (Fig. 5b,c) provide further support for the hypothesis that the lowest depth of

annual oscillation water table determines the depth of WF, previously based on shorter-term water table measurements and geochemical data[22]. As illustrated in Fig. 5g, the pyrite τ profiles (Methods) identified WF values of 4.0, 4.2 and 3.3 for sites PLM1, 2 and 3, respectively. These WF values are remarkably consistent with the water table depth minima at each of the locations (Fig. 5h). Through integrating mineralogic, hydrologic and geochemical including radiocarbon analyses we revealed that weathering is most active in the subsurface zone exposed to the oscillating water table. The water table minima can be used to predict the weathering front, shared by all the oxidation-dependent reactions (sulfide, IC_{rock} and OC_{rock}; Fig. 5b,c), with differences among reaction rates reflected in depletion profiles (Fig. 3e–g). It is worth noting that kinetic limitations (including physical protection)[6,50] and influx of oxygenated groundwaters[27,51] contribute to deviations from this pattern in other environments. Here reducing conditions observed below the water table[22] indicate that microbial respiration depletes the diffusive supply of O_2, thereby preventing pyrite oxidation.

Discussion

In this hillslope, C_{rock} is released at the rate of 9.8 Mg km² yr⁻¹, with 82% emitted as CO_2 (Fig. 6a). The remaining 18% is discharged through pore waters, mostly as DIC_{rock} for later transformation to CO_2 in oceans. All fluxes shown in this C balance diagram were calculated from measurements, except for the modern CO_2 influx from photosynthesis, which was assumed equal to the measured modern CO_2 efflux from respiration. It should be noted that these two C_{modern} rates are only included for completeness and do not affect the absolute values of C_{rock} flux calculations. It is also worth noting that release rates of rock CO_2 are substantially lower in grey shales such as those of in the Shale Hills catchment because of their low bedrock OC_{rock} concentrations[9]. Given that the East River's bedrock composition is typical of shales[52], the representativeness of the hillslope's C_{rock} releases can be evaluated

through a comparison with estimates of global C_{rock} weathering rates averaged per unit area.

A comparison with global estimates of C_{rock} fluxes from mountainous areas is warranted given that these regions are considered primarily responsible for terrestrial C_{rock} exports[1,4–8,15]. Estimates of global C_{rock} releases range from 80 to 160 Mt yr^{-1} (refs. 1,6). Normalizing these estimates by the global terrestrial shale area[5] of 3.42×10^7 km^2, results in global average shale C_{rock} release rates per unit area of 2.3 to 4.7 Mg km^2 yr^{-1}. However, mountainous regions globally are the source for about 63% of discharge, while comprising only 32% of the terrestrial surface area[53]. Scaling the global average shale C_{rock} release rates by these factors leads to average shale C_{rock} release rates from mountainous regions of 4.6 to 9.2 Mg km^2 yr^{-1}. These global and hillslope (9.8 Mg km^2 yr^{-1}) release rates are remarkably consistent and support the broad importance of subsurface flow within oxidizing weathering zones for releasing C_{rock} in mountainous regions.

Whereas Ganges floodplain solute release rates were found to be higher than those of their Himalayan source areas[54], other studies have reported disproportionately greater weathering in mountainous watersheds[1,4–8,15]. In such regions receiving higher precipitation, C_{rock} releases may be more sensitive to climate change than the more areally extensive basin regions. Indeed, climate change is already increasing the frequency of consecutive snow drought years[55,56], a condition that will drive the water table deeper, into previously permanently saturated bedrock (Fig. 6b). Such water table excursions deeper into the bedrock have been hypothesized to increase rates of oxidative weathering[33,50]. Whereas water table lowering will release more CO_2(rock) to the atmosphere from unsaturated bedrock, predicting its impacts on DIC_{rock} and DOC_{rock} exports into rivers is challenging because these depend on recharge, which is projected to decrease under climate change[57]. Nevertheless, C_{rock} weathering and export are clearly controlled by climate via subsurface hydrologic regulation of oxygen availability and transport rates (Fig. 6b, Extended Data Fig. 1 and Extended Data Tables 2 and 3). The approaches used here can be applied in other environments, integrating chemical analyses of hillslope profiles with subsurface hydrological analyses to further understand chemical weathering, weathering product exports into rivers and C_{rock} contributions to the global C cycle.

Methods

The study site

The site is located 3.8 km east–southeast of Snodgrass Mountain, Colorado, in the Rocky Mountains of the United States. The field study was conducted on a lower montane hillslope of the East River (ER) watershed underlain by Mancos Shale, with intensive sampling and monitoring within the lower 140 m section of a transect that extends nearly 1 km to its peak (Fig. 1c). The hillslope drains into the ER, which flows into the Gunnison River, a major tributary of the Colorado River. The ER contributes to 25% of the Gunnison River's discharge, which in turn contributes to 40% of the Colorado River's discharge[58,59]. Cretaceous Mancos Shale is a dominant lithology in the region[60], and solutes released by shale weathering strongly influence the chemistry of the ER Colorado River waters[60–62]. The composition of the hillslope's unweathered bedrock is typical of shales[5,52,63], with $1.46 \pm 0.40\%$ IC_{rock} and $1.53 \pm 0.15\%$ OC_{rock} (including the kerogen hotspots), $4.1 \pm 3.5\%$ pyrite, $1.8 \pm 2.2\%$ calcite and $7.5 \pm 1.6\%$ dolomite[22]. The hillslope is vegetated with shallow rooted grasses and forbs, and its subsurface consists of 1.0 ± 0.3 m thick loam to silt loam soil, underlain by weathered and fractured Mancos Shale bedrock. The area's climate is continental subarctic, with a mean annual precipitation about 600 mm with about 70% as snow. The ground is generally snow covered from November through early May, and monsoonal rains usually fall from mid-July to September.

Borehole drilling and instrumentation

Except for PLM6, all the boreholes (0.254 m diameter) were drilled using waterless sonic drilling[64], which allows drilling through the bedrock and recovery of depth-stratified samples of rock chips for laboratory analyses. Soil samples were obtained within several metres of drilled boreholes, by coring (0.10 m diameter) to as deep as the hand-auger could be advanced, in 0.10 to 0.15 m depth intervals. The average soil depth is 1.0 ± 0.3 m, based on 40 sampling holes along the hillslope.

To track subsurface water flow and biogeochemical reactions, three of the five boreholes (PLM 1, 2 and 3) were instrumented with sensors for measuring pressure, matric potential, moisture and temperature and samplers for collecting pore waters and pore gases[65]. The outlets of the samplers are set about 1.5 m above the ground surface, designed for collecting pore-water and pore-gas samples even during the winter snow seasons. Through these instruments, we obtained five years of time- and depth-dependent hydrologic and biogeochemical measurements of pore-water and pore-gas samples. It is worth noting that these pore-water, pore-gas and solid samples retain highly localize chemistry, in contrast to samples from the river that integrate inputs from the whole watershed upstream of the collection point. The water table depths were continuously recorded with pressure transducers (AquaTROLL 200) and also determined from equilibrium pressure measurements in pore-water samplers using the 'tensisampler' method[66] and from depth-distributed moisture sensors.

Sampling of different phases

In the laboratory, a 4.75 mm sieve was used to remove roots and coarser gravel from soil samples. The rock samples were collected at intervals of 50 cm and larger. All soil and the rock samples were oven dried at 105 °C for three days, then powdered to ≤50 μm for later analyses. Porewaters were collected with depth-distributed suction/pressure samplers (Soil-moisture Equipment Corp., 1920F1L06-B02M2) biweekly in spring and monthly at other times except when the ground was frozen.

The collected water samples were filtered in the field through 0.45 μm polytetrafluoroethylene syringe filters (Pall, 0.45 μm). Each of the filtered water samples was divided into subsamples for different types of analysis, including cation analysis (acidified immediately and stored in polyethylene vials), anion analysis, DOC and DIC analyses (collected in 40-ml glass vials, filled to eliminate headspace air). The water samples were kept in a cooler packed with coolant, shipped to the laboratory overnight and stored in a refrigerator for later analyses. Spatial variability in solute concentrations within each zone reflects the fact that individual pore water sample volumes typically range from 100 to 200 ml, largely collected from regions extending only several cm beyond the sampler's intake surface[67]. Therefore, samplers embedded in locations undergoing more active weathering are generally expected to yield higher concentrations of weathering products, whereas dilution from recharge waters (and from sulfate reduction) has the opposite effect[68]. Therefore, for each sampling time, solute concentrations obtained from multiple samplers within a given zone were averaged to obtain representative values.

The pore-gas samples were collected through custom-built pore-gas samplers[65]. At the field the extracted gas from a specific depth was injected (slightly over-pressurized) through a 14 mm-thick chlorobutyl septa into a pre-evacuated 50 ml serum glass vial (Bellco Glass Inc.).

Sample analyses

Soil and rock samples were analysed for elemental composition using X-ray fluorescence analyses by ALSGLOBAL-Geochemistry (http://www.alsglobal.com/geochemistry) in Reno, Nevada, United States. The analyses were conducted under ALS (Australian Laboratory Systems) code numbers ME-XRF26 and ME-ICP61 for 33 elements using four acid digestions and inductively coupled plasma atomic emission spectroscopy (ICP-AES), with uncertainty <0.1% based on three replicate measurements. Mineralogical compositions were determined by X-ray diffraction, by X-ray Mineral Services (http://www.xrayminerals.

co.uk) for both whole soil/rock samples and the clay fraction, with relative uncertainties <10%. Solid phase OC and IC were determined using a Shimadzu TOC-VCSH total organic and inorganic carbon analyser in our LBNL/EESA Aqueous Geochemistry Laboratory, with relative uncertainty <1%. For pore-water samples, the major and trace element cations were analysed using an inductively coupled plasma mass spectrometer (Thermo Fisher). The anions, Cl^-, NO_3^-, NO_2^-, SO_4^{2-}, PO_4^{3-} were measured by ion chromatograph (Dionex, ICS-2100, Thermo Scientific USA) with precisions of ±5% of reported values. DOC and DIC were determined using a TOC-VCPH analyser (Shimadzu Corporation). DOC was analysed as non-purgeable organic carbon by purging acidified samples with carbon-free air to remove DIC before measurement. For DOC and DIC measurements, relative standard deviation < 3% was estimated from 3–5 replicates. Pore-gas samples were analysed for CO_2, N_2O and CH_4 concentrations using a Shimadzu Gas Chromatograph (GC-2014), with a precision of ±5% of the reported value. More details can be found in our previous publications[22,28,69].

Radiocarbon sampling and analyses

Subsamples from the same powdered soil and rock samples used for elemental and mineral composition analyses were used for the analyses of $^{14}C(OC)$ compositions in solid phase. For dissolved carbon, $^{14}C(DOC)$ and $^{14}C(DIC)$ in pore waters, large quantities of pore waters were required, relative to the low volumetric yields of the pore-water samplers located above the water table. This is probably why data of this sort have not been previously available. Depending on carbon concentrations, 500 to 1,000 ml of pore water was needed for a sample. Below the water table, this quantity can be collected during a single sampling event. Above the water table, several successive sampling events are required to collect sufficient volumes of pore waters for a single analysis. The ^{14}C analyses in this paper are from several years of effort. $^{14}C(DOC)$ water samples were filtered and acidified in the field immediately after the collection with high purity hydrochloric acid to pH ~2.5 ± 0.3 and stored in glass bottles. $^{14}C(DIC)$ samples were 'poisoned' immediately after sampling by adding saturated $HgCl_2$ solution to kill the microorganisms and stored in glass bottles with no air space. Water samples were kept in a cooler with ice in the field and stored in a refrigerator in the laboratory before analyses. River water samples were collected directly downslope of the flow transect, downstream of PLM4. The $^{14}C(CO_2)$ analyses in gas phase requires 1 l of gas volume, collected in evacuated gastight 1,000-ml glass jars equipped with valves for connecting with the depth-distributed gas sampler outlets. Atmosphere air samples were collected at the hillslope near PLM1.

The solid phase $^{14}C(OC)$ and gas phase $^{14}C(CO_2)$ were analysed by the W.M. Keck Carbon Cycle Accelerator Mass Spectrometer Facility at the University of California, Irvine. Their protocols on sample preparation, analyses and reporting methods can be found at https://sites.uci.edu/keckams/protocols/. The compositions of pore-water $^{14}C(DOC)$ were analysed by the Woods Hole National Accelerator Mass Spectrometry Facility NOSAMS, following the protocols for sample preparation, analyses and data calculations at https://www2.whoi.edu/site/nosams/radiocarbon-services/. The concentrations of pore-water $^{14}C(DIC)$ were analysed by the Beta Analytics Radiocarbon Dating Service, and the method can be found at https://www.betalabservices.com/biobased/carbon14-dating.html/. Solid, water and gas ^{14}C results were corrected for isotopic fractionation according to the conventions of Stuiver and Polach[70], with $\delta^{13}C$ values measured on prepared graphite using the accelerator mass spectrometer. Sample preparation backgrounds were subtracted based on measurements of ^{14}C-free acid-washed coal. The ^{14}C concentrations are reported as fractions of the modern standard ^{14}C (Fm), following the conventions of Stuiver and Polach[70].

Water mass balance, subsurface flow and solute export

To analyse water mass balance and determine subsurface water fluxes, we used daily precipitation (P) data from the Butte SNOTEL station[71]

located 3.1 km south of the site. Because of interannual changes in subsurface water storage, annual subsurface flow is not simply equated with P minute evapotranspiration (ET). Instead, subsurface flow on an annual basis was equated with an effective annual precipitation (P′) minus ET. The influence of interannual subsurface water storage was approximated through allowing winter precipitation in excess of a threshold level snowpack precipitation P_{tsp} to contribute to effective precipitation in the following year. P_{tsp} was set to 505 mm through optimizing the hillslope water mass balance over five years with widely ranging annual P, resulting in 46 and 41 mm of P from high snow water years 2017 and 2019 being carried over to water years 2018 and 2020, respectively[33]. Correlations between air temperature data from the Butte SNOTEL station and ER-CSMWS were used to estimate the daily average, minimum and maximum air temperatures needed for calculating all daily ET with the Community Land Model (CLM)[72,73], except when snow cover was present. On days with snow covered ground, ET was assigned the average sublimation rate of 0.3 mm d^{-1} based on eddy covariance measurements reported in a study conducted at a different mountainous location in Colorado[74].

The water table elevations continuously recorded by piezometers are shown in Fig. 2b in the main text. Dividing the water table elevations between PLM1 and PLM3 locations by their horizontal separation distance of 137 m yields a continuous record of the hydraulic gradient driving downslope flow. These measurements show that the flows are approximately parallel to the hillslope's soil surface which has an average slope of 0.197 m m^{-1}. Therefore, flow within the saturated bedrock and variably saturated weathering zone and soil can be calculated using the Dupuit–Forchheimer approximation for flow along a sloping water table[75] with the unit normal area for groundwater flow being perpendicular to the slope. With this approximation, the cross-sectional area for flow is obtained through scaling down the saturated vertical thickness by $\cos\theta$, where θ is the slope between PLM1 and PLM3. With $\theta = 11.2°$, only a minor correction factor of $\cos\theta = 0.98$ is needed because of the moderate slope.

To calculate downslope flow, the daily average water table elevations along the hillslope are used by determining the saturated thickness within the weathering zone (wz, 1.00–3.60 m average depth) b_{wz} and within the two soil regions (s1, 0–0.50 m depth and s2, 0.50–1.00 m depth) b_{s1} and b_{s2}. Multiplying these $\cos\theta$-scaled thicknesses by the respective saturated K assigned to each layer, we obtained the respective transmissivities, T_{s1}, T_{s2} and T_{wz}. Note that the downslope flow along the soil is only effective when the water table resides within the soil such that $b_{si} > 0$, hence T_s is usually zero. Very deep flow cannot be quantified because boreholes were only drilled to 10.0 m below ground surface. Therefore, the transmissivity of the permanently saturated fractured bedrock T_{fbr} was among the parameters adjusted to match the estimated annual subsurface flux. The daily subsurface flow equated to the sum of the four T values times the hydraulic gradient (gradH), and these daily flows were summed to obtain yearly subsurface flow, Q_a.

$$Q_a = \sum_{day\,1}^{day\,365} (T_{s1} + T_{s1} + T_{wz} + T_{fbr})\,\text{gradH} \qquad (5)$$

The subsurface water fluxes were initially calculated with field-measured K_{s1}, K_{s2}, K_{wz} and K_{fbr}[65]. However, previous field studies showing that small-scale measurements substantially underestimate K at the hillslope scale[76–80]. On the basis of these considerations, all K values were varied while keeping the depth b_{fbr} at its original value to constraint the actual amounts of flows. Additional constraints include that $K_s > K_{wz} > K_{fbr}$, in keeping with original framework of the transmissivity feedback model. Daily water table-dependent transmissivity-based fluxes for all layers were summed on a yearly basis for WY2017 through WY2021. Because the effective depth of the flow domain is unknown, T_{fbr} rather than K_{fbr} was used for calculating flow through the bedrock. The variables K_{s1}, K_{s2}, K_{wz} and T_{fbr} were optimized

using the Solver regression tool in Microsoft Excel. Adjusting these K, T and P_{tsp} values to minimized deviations between annual calculated subsurface flow Q_a and $P_e - ET$ over the five years having widely varying P yielded values of K_{s1}, K_{s2} and K_{wz} equal to 1.4×10^{-5}, 2.7×10^{-4} and 3.9×10^{-6} m s^{-1}, $T_{fbr} = 2.3 \times 10^{-6}$ m^2 s^{-1} and $P_{tsp} = 508$ mm, respectively. These optimized values resulted in a small root mean-square deviation between Q_a and $P_e - ET$ of 43 mm (7% of the average annual P), despite encompassing years with near-record P and drought years.

Daily subsurface discharges of solute species 'i' were calculated by weighting interpolated zone-specific concentrations by their corresponding daily flow rates

$$q_i = (c_{i,s1}T_{s1} + c_{i,s2}T_{s2} + c_{i,wz}T_{wz} + c_{i,fbr}T_{fbr})\,\text{grad}H \qquad (6)$$

Equation (6) shows how flow in each active zone (when the water table height supports $b_i > 0$, hence $T_i > 0$) exerts a first-order impact on solute export.

Quantifying C$_{rock}$ release rates

Three approaches were used to estimate rates of IC$_{rock}$ weathering: sulfate discharge, base cation discharge and eroded IC$_{rock}$ profile reconstruction. Sulfate was not detectable in bedrock mineralogy nor in its water extracts, and atmospheric deposition in the region contributes only about 0.4 kmol S km^{-2} yr^{-1} (ref. [81]). Therefore, [SO$_4^{2-}$] measured in pore waters is attributed to pyrite dissolution in the weathering zone, and daily rates of [SO$_4^{2-}$] discharge were calculated based on equation (6). Sulfate dissolution is assumed to release equivalent amounts of IC$_{rock}$ based on the much higher dissolution rates of carbonate rocks relative to other minerals under acidic conditions[7,8,35].

Exports of base cations (BC = $\sum$(Na$^+$, K$^+$, Ca^{2+}, Mg^{2+})) are often used to characterize bedrock weathering, albeit indirectly from measurements in rivers[35–37]. We extended that method into the subsurface by tracking pore-water BC concentrations and flow within the soil, WZ and FBR using equation (6). To estimate IC$_{rock}$ weathering based on BC export rates, we assumed that IC$_{rock}$ weathers in proportion to the measured IC$_{rock}$:BC$_{rock}$ ratio of 0.32 mol mol$_c^{-1}$.

To estimate the rate of IC$_{rock}$ release, the profiles of S (Fig. 3e) and IC$_{rock}$ (Fig. 3f) were assumed to reflect their weathering from Mancos Shale at constant rates, which for S is taken as 394 kmol km^{-2} yr^{-1} based on five years of sulfate discharge measurements. For reconstructing the pre-erosion regolith to determine past S and IC$_{rock}$ losses, time zero was assigned to the retreat of the Pinedale Glacier from the hillslope, estimated at 16.0 ± 1.5 ka before present based on ages reported for neighbouring areas within the East River watershed[38]. Export of S over 16.0 ± 1.5 ka at the average rate of 394 kmol km^{-2} yr^{-1} amounts to 6.30 ± 0.59 kmol m^{-2}, equivalent to a bedrock weathering depth of 4.42 ± 0.41 m based on the unweathered shale S concentration of 1.43 kmol m^{-3}. Given the present-day S depletion depth of 3.60 m, about 0.82 ± 0.41 m of regolith has been eroded (Fig. 3e). The present-day weathering depleted IC$_{rock}$ equivalent depth is then added to the 0.82 m of erosively removed regolith to estimated total IC$_{rock}$ released.

Estimates of OC$_{rock}$ release were obtained with OC$_{rock}$ profiles, assuming OC$_{rock}$ weathering release at constant rate over a period of 16.0 ± 1.5 ka. Combining the present-day OC$_{rock}$ depletion profile equivalent of 1.15 m unweathered shale with 0.82 m of erosively removed regolith yields the estimated total OC$_{rock}$ released thickness of 1.97 m (Fig. 3g). The product of this total weathering thickness times the unweathered shale OC$_{rock}$ concentration of 3,180 mol m^{-3} was divided by 16,000 years to obtain the average OC$_{rock}$ release rate of 392 ± 37 kmol km^{-2} yr^{-1}.

Quantifying CO$_2$ diffusion rates

Total porosities, matric potentials and volumetric water contents (Fig. 4e) needed for calculating the effective diffusion coefficient were obtained from core sample measurements at adjacent locations and from sensors (Decagon 5TE and MPS6), respectively[82]. Daily average soil temperature (Fig. 4f) measured by the shallowest matric potential sensor (Decagon MPS6) and an average local atmospheric pressure of 72 KPa (estimated with the Boltzmann barometric equation for the average hillslope elevation of 2,776 m) were applied to Massman's CO$_2$ D_o formula[82,83]. Specific values for Φ for the midplane of the shallowest interval at PLM1, PLM2 and PLM3 were assigned 0.58, 0.59 and 0.63, respectively, based on a polynomial fit of data on the depth dependence of shallow soil bulk densities and an assumed solid density of 2.65 g cm^{-3}. Values for the CO$_2$ effective diffusion coefficient D_e (Fig. 4g) were then calculated with the water-induced linear reduction model applied to Marshall's model[84],

$$D_e = D_o \varepsilon^{2.5}\Phi^{-1} \qquad (7)$$

where Φ is the total porosity, ε is the air-filled porosity (Φ minus the volumetric soil water content) and D_o is the pressure- and temperature-dependent diffusion coefficient for CO$_2$ in the bulk air phase. In the absence of snow cover, the CO$_2$ concentrations measured in the shallowest pore-gas samplers (Fig. 4h), and atmosphere samples were used to calculate the concentration gradient (Fig. 4i) for diffusion calculations based on Fick's law[82].

During winter time with snowpack, diffusive resistance within the snow cover causes CO$_2$ concentrations to increase above 420 ppm at the soil–snow interface, and the interface CO$_2$ concentration requires estimation. For negligible storage within the snowpack, the diffusive fluxes of CO$_2$ through the surface soil and snowpack are approximated as equal.

$$D_e \frac{(C_1 - C_b)}{z_1} = D_{snow}\frac{(C_b - C_0)}{z_2} \qquad (8)$$

where C_1, C_b and C_0 are the CO$_2$ concentrations in the shallowest gas sampler (Fig. 4h), at the soil–snow boundary and in the atmosphere (420 ppm), respectively, D_{snow} is the effective diffusion coefficient of CO$_2$ through snow, and z_1 and z_2 are the depth of the shallowest soil gas sampler and the thickness of the snowpack, respectively. Values of D_{snow} were estimate based on the linear reduction model (equation (7)), with ε identical to Φ_{snow}, using daily snow densities measured at the nearby snow telemetry station (Butte SNOTEL). The snowpack thicknesses z_2 were estimated from a linear regression between measurements obtained along the hillslope transect during winters of 2017 and 2021, and thicknesses reported for the Butte SNOTEL. Values of C_b were calculated for steady-state diffusion in series through the surface soil and snowpack as

$$C_b = \left(\frac{z_2 D_e}{z_1 D_{snow} + z_2 D_e}\right)C_1 + \left(\frac{z_1 D_{snow}}{z_1 D_{snow} + z_2 D_e}\right)C_0 \qquad (9)$$

It should be noted that the calculated diffusive fluxes may be underestimates because wind can enhance gas fluxes through snow[85].

CO$_2$ fluxes were calculated as the product of the D_e and the CO$_2$ concentration gradient within the surface soil on a daily basis by applying Fick's law. Daily diffusive fluxes based on a given gas sampling date were applied backwards and forwards in time to midpoints between actual measurement days to interpolate between measured days. For the large data gap (September 2018 through May 2019) when samples were not available, the average of all measured gradients was used for the location.

Direct CO$_2$ flux measurements were obtained during summer of 2018 with flux chambers (Li-Cor Biosciences LI-8100A) multiplexed (LI-8150) to 0.203 m inner diameter collars embedded into the surface soils at three locations within each of the hillslope stations (PLM1, PLM2 and PLM3). The measurement system was powered by a stationary set of

batteries and solar panels, and flux chambers were moved sequentially to each of the PLM stations. At each of the stations, CO_2 fluxes were cyclically measured (measurement durations of 2 min, 20 min between measurements) on three collars over total run times of 3 to 5 days. It should be noted that recent studies indicates that flux chamber measurements can yield overestimates of CO_2 effluxes when steady-state conditions are not established[86].

Quantifying CO_2 losses originating from C_{rock}

The total CO_2 efflux originating from C_{rock} was obtained from the sum of IC_{rock} and OC_{rock} contributions. The rate of CO_2 release originating from IC_{rock} was calculated by subtracting the rate of DIC_{rock} export from the IC_{rock} weathering release rate. Likewise, the CO_2 release originating from OC_{rock} oxidation was calculated by subtracting the rate of DOC_{rock} export from the OC_{rock} weathering release rate.

Contribution of OC_{bio} ageing

At this site soil contains shallow roots and shale is the parent rock (Extended Data Fig. 1a shows unweathered shale fragments in soil). The soil contained OC is a mixture of OC_{rock} ($Fm_{rock} = 0$) and biosphere OC_{bio} ($Fm_{bio} \leq 1.0$, because OC_{bio} starts ageing after its formation[46,47]). The very high $OC_{bio}\%$ appear in the surface soil, where $Fm_{bulk} = 1.0$. The $OC_{bio}\%$ together with Fm_{bulk} rapidly decrease as the depth and reach to $OC_{bio}\% = 0$ and $Fm_{bulk} = 0$ at depth about 2.0 m (Extended Data Fig. 1b,c). To estimate the Fm_{bio} at the depth above 2.0 m, we adapted two approaches by Galy et al.[17] and Torres et al.[48]. They proposed that the particulates OC (POC) in riverine sediments are the mixture of ancient petrogenic OC_{rock} ($Fm_{rock} = 0.0$) and OC_{bio} (Fm_{bio} values unknown) and derived models for estimating Fm_{bio} values in riverine POC. Applying the approach of Galy et al.[17]

$$Fm_{bulk} \times OC_{bulk}\% = Fm_{bio} \times OC_{bulk}\% - Fm_{bio} \times OC_{rock}\% \quad (10)$$

using measured Fm_{bulk} and $OC_{bulk}\%$, we plotted the relations of $Fm_{bulk} \times OC_{bulk}\%$ vs $OC_{bulk}\%$ (Extended Data Fig. 1d). In this plot the data points from samples shallower than 2 m fall along a single trendline (equation (11)) with $r^2 = 0.99$, indicating mixing of two pure ^{14}C end members. The data below about 2.0 m distribute along the x axis, indicating 100% OC_{rock}.

$$Y = 1.09X - 1.05 \quad (11)$$

Comparing equations (10) and (11), we obtained $Fm_{bio} \approx 1.09$, showing that Fm_{bio} is practically modern. The intercept value of −1.05 matches the $OC_{rock}\%$ of the bedrock at and below 2.0 m (Extended Data Fig. 1b). We also applied the approach from Torres et al.[48].

$$Fm_{bulk} = [Fm_{bio} \times ([OC\%]_{bulk} - [OC\%]_{rock})] / [OC\%]_{bulk} \quad (12)$$

where Fm_{bulk}, $[OC\%]_{bulk}$ and $[OC\%]_{rock}$ are measurements. Note that $[OC]_{rock}$ is represented by the average in the bedrock (Extended Data Fig. 1b). The calculations resulted in $Fm_{bio} = 1.18 \pm 0.10$, again showed that Fm_{bio} is practically modern. Whereas ageing of OC_{bio} is certainly occurring[87], the integrated rates of its synthesis and degradation determines the overall age of accumulated OC_{bio}. These analyses support the two end members mixing approach as a reasonable approximation for this system.

Pyrite relative concentrations

The relative concentration $\tau_{i,j}$[2,88] defined by equation (13) for a given depth is used to evaluate loss of an element or mineral relative to the unweathered parent rock caused by weathering

$$\tau_{i,j} = \frac{C_{j,w} C_{i,p}}{C_{j,p} C_{i,w}} - 1 \quad (13)$$

where c represents concentration, the subscript j represents a mobile constituent (element or mineral of interest) and subscript i represents the selected immobile reference element associated with the parent rock. The subscripts w and p denote weathered and parent rock, respectively. In our calculations the pyrite concentrations in weathered and parent rock were measured depth profiles from the three boreholes, PLM 1, 2 and 3. The value of parent rock pyrite concentration was determined by averaging the data at the depth below about 4.0 m from the three boreholes. Titanium (Ti) was used as the immobile refs. 2,88. By following this approach, the weathering zone (WZ) can be defined as the depth region between $-1 < \tau < 0$. The weathering front (WF) is defined by the depth at which $\tau = 0$.

Calculating C_{rock} in groundwater discharge

Because large volumes of pore-water samples needed for ^{14}C analyses could only be collected infrequently, temporal trends of [14]C Fm within the soil, weathering zone and bedrock pore waters were not obtained. Instead, average values of Fm(DOC) and Fm(DIC) within each of these zones were used. Averages of Fm for DOC in soil, WZ and FBR are 0.95 ± 0.07, 0.51 ± 0.13 and 0.74 ± 0.11, respectively. Averages of [14]C Fm for DIC measured in pore waters of soil, WZ and FBR are 0.97 ± 0.04, 0.77 ± 0.22 and 0.59 ± 0.08, respectively. These average FM were multiplied by daily flow rates within their corresponding zones to obtain flow-weighted overall [14]C Fm of DOC and DIC exported from the hillslope (Fig. 5e,f). Over the course of five years, the resulting average [14]C Fm(DOC) and [14]C Fm(DIC) are 0.81 ± 0.14 and 0.79 ± 0.08 respectively.

Hillslope carbon mass balance

Essential background information used for determining fluxes of carbon in the hillslope and the component C influxes and effluxes and their measurement sources are presented through three tables. Extended Data Table 1 summarizes average properties of the Mancos Shale bedrock, subsurface flow and weathering rates. Extended Data Tables 2 and 3 summarize C influxes and effluxes, respectively. It should be noted that only the photosynthetic input of C included in Extended Data Table 2 is estimated (assuming balance with modern C effluxes), and none of the other fluxes depend on that estimate.

Major sources of uncertainty

Data needed for calculating weathering fluxes can be broadly categorized into chemical/mineralogical analyses and hydrologic. Given that the chemical/mineralogical analyses involved in this study all follow standard procedures with quality control assuring small relative uncertainties (generally much smaller than 5%), the greatest uncertainties in calculations are expected to be associated with hydrologic inputs.

Given the central role of the hydrologic cycle in driving weathering, the most basic uncertainties in modelling the processes presented here concern quantification of subsurface discharge, which in turn is determined from the differences between precipitation and evapotranspiration. The details of that treatment were presented in Tokunaga et al.[33] and the uncertainties are reviewed here. The Butte SNOTEL station, located 3 km away from the hillslope site, was used for its continuous record of precipitation and other meteorological parameters needed for calculations of evapotranspiration. The next closest weather station at Gothic, 5 km away in the opposite direction from the field site records precipitation amounts that are about 20% greater than those recorded at the Butte SNOTEL. Given that our field site is approximately midway between the two weather stations and at an intermediate elevation, we expect that the uncertainty in daily precipitation for the site is about 10%.

Unlike measured precipitation, evapotranspiration (ET) rates were obtained from calculations based on the Community Land Model CLM[73], with input parameters from the Butte SNOTEL and the hillslope transect. Whereas the CLM has been widely used in a variety

of environments, it is noteworthy that CLM-predicted ET agrees well with direct soil water mass balances measured at the East River hillslope site[33]. Analyses of annual precipitation minus calculated annual ET showed that residual subsurface groundwater storage from high snowmelt years needs to be carried over to the following water year to achieve consistent water mass balance. A carry-over of 46 mm (WY2017 into WY2018) and 41 mm (WY2019 into WY2020) combined with calibrating hydraulic conductivity and transmissivity values optimized the total water mass balance, with a root mean-square deviation of 40 mm over the five water years. This deviation amounts to 24% of the average annual discharge.

Given the low porosity of snowpacks, the greatest uncertainties in diffusive CO_2 fluxes are probably from possible wind-induced advection effects that could enhance releases during periods with snow cover[28]. Given the greater diffusive resistance provided in the underlying soil zone, the wind-induced enhancement in CO_2 efflux is not expected to exceed 10%.

Data availability
Data used in this paper have been placed in the US Department of Energy's Environmental Systems Science Data Infrastructure for a Virtual Ecosystem (ESS-DIVE), accessible at https://doi.org/10.15485/2322567.

References
1. Hilton, R. G. & West, A. J. Mountains, erosion and the carbon cycle. *Nat. Rev. Earth Env.* **1**, 284–299 (2020).
2. Anderson, S. P., Dietrich, W. E. & Brimhall, G. H. Weathering profiles, mass-balance analysis, and rates of solute loss: linkages between weathering and erosion in a small, steep catchment. *Geol. Soc. Am. Bull.* **114**, 1143–1158 (2002).
3. Wilson, M. J. Weathering of the primary rock-forming minerals: processes, products and rates. *Clay Miner.* **39**, 233–266 (2004).
4. Torres, M. A. et al. The acid and alkalinity budgets of weathering in the Andes-Amazon system: insights into the erosional control of global biogeochemical cycles. *Earth Planet. Sci. Lett.* **450**, 381–391 (2016).
5. Amiotte Suchet, P., Probst, J. L. & Ludwig, W. Worldwide distribution of continental rock lithology: implications for the atmospheric/soil CO_2 uptake by continental weathering and alkalinity river transport to the oceans. *Glob. Biogeochem. Cycles* **17**, 1038 (2003).
6. Petsch, S. T. in *Treatise on Geochemistry* Vol. 12.8 (eds Turekian, K. & Holland, H.) 217–238 (Elsevier, 2014).
7. Torres, M. A., West, A. J. & Li, G. J. Sulphide oxidation and carbonate dissolution as a source of CO_2 over geological timescales. *Nature* **507**, 346 (2014).
8. Calmels, D., Gaillardet, J., Brenot, A. & France-Lanord, C. Sustained sulfide oxidation by physical erosion processes in the Mackenzie River basin: climatic perspectives. *Geology* **35**, 1003–1006 (2007).
9. Jin, L. X. et al. The CO_2 consumption potential during gray shale weathering: insights from the evolution of carbon isotopes in the Susquehanna Shale Hills critical zone observatory. *Geochim. Cosmochim. Acta* **142**, 260–280 (2014).
10. Petsch, S. T., Edwards, K. J. & Eglinton, T. I. Microbial transformations of organic matter in black shales and implications for global biogeochemical cycles. *Palaeogeogr. Palaeoclimatol. Palaeoecol.* **219**, 157–170 (2005).
11. Hemingway, J. D. et al. Microbial oxidation of lithospheric organic carbon in rapidly eroding tropical mountain soils. *Science* **360**, 209 (2018).
12. Lerman, A., Wu, L. L. & Mackenzie, F. T. CO_2 and H_2SO_4 consumption in weathering and material transport to the ocean, and their role in the global carbon balance. *Mar. Chem.* **106**, 326–350 (2007).
13. Gabet, E. J. & Mudd, S. M. A theoretical model coupling chemical weathering rates with denudation rates. *Geology* **37**, 151–154 (2009).
14. Hilton, R. G., Galy, A. & Hovius, N. Riverine particulate organic carbon from an active mountain belt: Importance of landslides. *Glob. Biogeochem. Cycles* https://doi.org/10.1029/2006gb002905 (2008).
15. Das, A., Chung, C. H. & You, C. F. Disproportionately high rates of sulfide oxidation from mountainous river basins of Taiwan orogeny: sulfur isotope evidence. *Geophys. Res. Lett.* https://doi.org/10.1029/2012gl051549 (2012).
16. Hilton, R. G. et al. Concentration-discharge relationships of dissolved rhenium in alpine catchments reveal its use as a tracer of oxidative weathering. *Water Resour. Res.* https://doi.org/10.1029/2021WR029844 (2021).
17. Galy, V., Beyssac, O., France-Lanord, C. & Eglinton, T. Recycling of graphite during himalayan erosion: a geological stabilization of carbon in the crust. *Science* **322**, 943–945 (2008).
18. Tune, A. K., Druhan, J. L., Lawrence, C. R. & Rempea, D. M. Deep root activity overprints weathering of petrogenic organic carbon in shale. *Earth Planet. Sci. Lett.* **607**, 118048 (2023).
19. West, A. J. Thickness of the chemical weathering zone and implications for erosional and climatic drivers of weathering and for carbon-cycle feedbacks. *Geology* **40**, 811–814 (2012).
20. Brantley, S. L. et al. Toward a conceptual model relating chemical reaction fronts to water flow paths in hills. *Geomorphology* **277**, 100–117 (2017).
21. Lebedeva, M. I. & Brantley, S. L. Relating the depth of the water table to the depth of weathering. *Earth Surf. Processes Landforms* **45**, 2167–2178 (2020).
22. Wan, J. et al. Predicting sedimentary bedrock subsurface weathering fronts and weathering rates. *Sci. Rep.* https://doi.org/10.1038/s41598-019-53205-2 (2019).
23. Rempe, D. M. & Dietrich, W. E. Direct observations of rock moisture, a hidden component of the hydrologic cycle. *Proc. Natl Acad. Sci. USA* **115**, 2664–2669 (2018).
24. Tune, A. K., Druhan, J. L., Wang, J., Bennett, P. C. & Rempe, D. M. Carbon dioxide production in bedrock beneath soils substantially contributes to forest carbon cycling. *J. Geophys. Res. G: Biogeosci.* https://doi.org/10.1029/2020JG005795 (2020).
25. Salve, R., Rempe, D. M. & Dietrich, W. E. Rain, rock moisture dynamics, and the rapid response of perched groundwater in weathered, fractured argillite underlying a steep hillslope. *Water Resour. Res.* **48**, W11528 (2012).
26. Anderson, S. P. & Dietrich, W. E. Chemical weathering and runoff chemistry in a steep headwater catchment. *Hydrol. Processes* **15**, 1791–1815 (2001).
27. Brantley, S. L., Holleran, M. E., Jin, L. X. & Bazilevskaya, E. Probing deep weathering in the Shale Hills Critical Zone Observatory, Pennsylvania (USA): the hypothesis of nested chemical reaction fronts in the subsurface. *Earth Surf. Processes Landforms* **38**, 1280–1298 (2013).
28. Wan, J. et al. Bedrock weathering contributes to subsurface reactive nitrogen and nitrous oxide emissions. *Nat. Geosci.* **14**, 217 (2021).
29. Soulet, G. et al. Temperature control on CO_2 emissions from the weathering of sedimentary rocks. *Nat. Geosci.* **14**, 665–66 (2021).
30. Sullivan, P. L. et al. Oxidative dissolution under the channel leads geomorphological evolution at the Shale Hills catchment. *Am. J. Sci.* **316**, 981–1026 (2016).
31. Winnick, M. J. et al. Snowmelt controls on concentration-discharge relationships and the balance of oxidative and acid-base weathering fluxes in an alpine catchment, East River, Colorado. *Water Resour. Res.* **53**, 2507–2523 (2017).

32. Torres, M. A., West, A. J. & Clark, K. E. Geomorphic regime modulates hydrologic control of chemical weathering in the Andes-Amazon. *Geochim. Cosmochim. Acta* **166**, 105–128 (2015).

33. Tokunaga, T. K. et al. Quantifying subsurface flow and solute transport in a snowmelt-recharged hillslope with multiyear water balance. *Water Resour. Res.* **58**, e2022WR032902 (2022).

34. Bishop, K., Seibert, J., Nyberg, L. & Rodhe, A. Water storage in a till catchment. II: implications of transmissivity feedback for flow paths and turnover times. *Hydrol. Processes* **25**, 3950–3959 (2011).

35. Langmuir, D. *Aqueous Environmental Geochemistry* (Prentice-Hall, 1997).

36. Horton, T. W., Chamberlain, C. P., Fantle, M. & Blum, J. D. Chemical weathering and lithologic controls of water chemistry in a high-elevation river system: Clark's Fork of the Yellowstone River, Wyoming and Montana. *Water Resour. Res.* **35**, 1643–1655 (1999).

37. Anderson, S. P., Drever, J. I. & Humphrey, N. F. Chemical weathering in glacial environments. *Geology* **25**, 399–402 (1997).

38. Quirk, B. J., Larsen, I. J. & Hidy, A. J. Latest Pleistocene glacial chronology and paleoclimate reconstruction for the East River watershed, Colorado, USA. *Quat. Res.* **119**, 86–98 (2024).

39. Smith, M. E., Carroll, A. R. & Mueller, E. R. Elevated weathering rates in the Rocky Mountains during the Early Eocene Climatic Optimum. *Nat. Geosci.* **1**, 370–374 (2008).

40. Foster, M. A., Anderson, R. S., Wyshnytzky, C. E., Ouimet, W. B. & Dethier, D. P. Hillslope lowering rates and mobile-regolith residence times from in situ and meteoric Be-10 analysis, Boulder Creek Critical Zone Observatory, Colorado. *Geol. Soc. Am. Bull.* **127**, 862–878 (2015).

41. Wildman, R. A. et al. The weathering of sedimentary organic matter as a control on atmospheric O_2: I. analysis of a black shale. *Am. J. Sci.* **304**, 234–249 (2004).

42. Gu, X. & Brantley, S. L. How particle size influences oxidation of ancient organic matter during weathering of black shale. *ACS Earth Space Chem.* **6**, 1443–1459 (2022).

43. Shaughnessy, A. R. & Brantley, S. L. How do silicate weathering rates in shales respond to climate and erosion? *Chem. Geol.* https://doi.org/10.1016/j.chemgeo.2023.121474 (2023).

44. Zhao, Z. Y. et al. Model prediction of biome-specific global soil respiration from 1960 to 2012. *Earth's Future* **5**, 715–729 (2017).

45. Raich, J. W. & Schlesinger, W. H. The global carbon-dioxide flux in soil respiration and Its relationship to vegetation and climate. *Tellus B* **44**, 81–99 (1992).

46. Lawrence, C. R., Harden, J. W., Xu, X. M., Schulz, M. S. & Trumbore, S. E. Long-term controls on soil organic carbon with depth and time: a case study from the Cowlitz River Chronosequence, WA USA. *Geoderma* **247**, 73–87 (2015).

47. Torn, M. S., Trumbore, S. E., Chadwick, O. A., Vitousek, P. M. & Hendrick, D. M. Mineral control of soil organic carbon storage and turnover. *Nature* **389**, 170–173 (1997).

48. Torres, M. A. et al. Model predictions of long-lived storage of organic carbon in river deposits. *Earth Surf. Dyn.* **5**, 711–730 (2017).

49. Carroll, R. W. H. et al. Factors controlling seasonal groundwater and solute flux from snow-dominated basins. *Hydrol. Processes* **32**, 2187–2202 (2018).

50. Manning, A. H., Verplanck, P. L., Caine, J. S. & Todd, A. S. Links between climate change, water-table depth, and water chemistry in a mineralized mountain watershed. *Appl. Geochem.* **37**, 64–78 (2013).

51. Liao, R. X., Gu, X. & Brantley, S. L. Weathering of chlorite from grain to watershed: the role and distribution of oxidation reactions in the subsurface. *Geochim. Cosmochim. Acta* **333**, 284–307 (2022).

52. Copard, Y., Amiotte-Suchet, P. & Di-Giovanni, C. Storage and release of fossil organic carbon related to weathering of sedimentary rocks. *Earth Planet. Sci. Lett.* **258**, 345–357 (2007).

53. Viviroli, D., Weingartner, R. & Messerli, B. Assessing the hydrological significance of the world's mountains. *Mt. Res. Dev.* **23**, 32–40 (2003).

54. Bickle, M. J. et al. Chemical weathering outputs from the flood plain of the Ganga. *Geochim. Cosmochim. Acta* **225**, 146–175 (2018).

55. Marshall, A. M., Abatzoglou, J. T., Link, T. E. & Tennant, C. J. Projected changes in interannual variability of peak snowpack amount and timing in the western United States. *Geophys. Res. Lett.* **46**, 8882–8892 (2019).

56. Alvarez-Garreton, C., Boisier, J. P., Garreaud, R., Seibert, J. & Vis, M. Progressive water deficits during multiyear droughts in basins with long hydrological memory in Chile. *Hydrol. Earth Syst. Sci.* **25**, 429–446 (2021).

57. Miller, O. L. et al. How will baseflow respond to climate change in the Upper Colorado River Basin? *Geophys. Res. Lett.* https://doi.org/10.1029/2021GL095085 (2021).

58. Ugland, R. C., Cochran, B. J., Kretschman, R. G., Wilson, E. A. & Bennett, J. D. *Water Resources Data, Colorado, Water Year 1990, Vol. 2. Colorado River Basin* Water Data Report CO-90-2 (US Geological Survey, 1991).

59. Spahr, N. E., Boulger, R. W. & Szmajter, R. J. *Water Quality at Basic Fixed Sites in the Upper Colorado River Basin National Water-Quality Assessment Study Unit, October 1995–September 1998* Water Resource Investigations Report 99-4223 (US Geological Survey, 1999).

60. Morrison, S. J., Goodknight, C. S., Tigar, A. D., Bush, R. P. & Gil, A. Naturally occurring contamination in the Mancos Shale. *Environ. Sci. Technol.* **46**, 1379–1387 (2012).

61. Winnick, M. et al. Snowmelt controls on concentration-discharge relationships and the balance of oxidative and acid-base weathering fluxes in an alpine catchment, East River, Colorado. *Water Resour. Res.* **53**, 2507–2523 (2017).

62. Carroll, R. W. H. et al. Factors controlling seasonal groundwater and solute flux from snow-dominated basins. *Hydrol. Processes* **32**, 2187–2202 (2017).

63. Shaw, D. B. & Weaver, C. E. Mineralogical Composition of Shales. *J. Sediment. Petrol.* **35**, 213–21 (1965).

64. *Standard Practices for Sonic Drilling for Site Characterization and Installation of Subsurface Monitoring Devices* ASTM **D 6914-04**, 1-11 (ASTM, 2004).

65. Tokunaga, T. K. et al. Depth- and time-resolved distributions of snowmelt-driven hillslope subsurface flow and transport and their contributions to surface waters. *Water Resour. Res.* **55**, 9474–9499 (2019).

66. Tokunaga, T. The pressure response of the soil water sampler and possibilities for simultaneous soil solution sampling and tensiometry. *Soil Sci.* **154**, 171–183 (1992).

67. Wu, L., Baker, J. M. & Allmaras, R. R. Numerical and field evaluation of soil water sampled by suction lysimeters. *J. Environ. Qual.* **24**, 147–152 (1995).

68. Netto, A. M., Pieritz, R. A. & Gaudet, J. P. Field study on the local variability of soil water content and solute concentration. *J. Hydrol.* **215**, 23–37 (1999).

69. Wan, J. M. et al. Deep unsaturated zone contributions to carbon cycling in semiarid environments. *J. Geophys. Res. Biogeosci.* **123**, 3045–3054 (2018).

70. Stuiver, M. & Polach, H. A. Reporting of C-14 data—discussion. *Radiocarbon* **19**, 355–363 (1977).

71. *Colorado SNOTEL Site Butte (380)* (USDA, 2021); https://wcc.sc.egov.usda.gov/nwcc/site?sitenum=380

72. Oleson, K. W. et al. *Technical Description of Version 4.5 of the Community Land Model (CLM)* 434 (National Center for Atmospheric Research, 2013).

73. Tran, A. P., Rungee, J., Faybishenko, B., Dafflon, B. & Hubbard, S. S. Assessment of spatiotemporal variability of evapotranspiration and its governing factors in a mountainous watershed. *Water* **11**, 243 (2019).

74. Sexstone, G. A., Clow, D. W., Stannard, D. I. & Fassnacht, S. R. Comparison of methods for quantifying surface sublimation over seasonally snow-covered terrain. *Hydrol. Processes* **30**, 3373–3389 (2016).

75. Childs, E. C. Drainage of groundwater resting on a sloping bed. *Water Resour. Res.* **7**, 1256–1263 (1971).

76. Brooks, E. S., Boll, J. & McDaniel, P. A. A hillslope-scale experiment to measure lateral saturated hydraulic conductivity. *Water Resour. Res.* **40**, W04208 (2004).

77. Di Prima, S., Marrosu, R., Lassabatere, L., Angulo-Jaramillo, R. & Pirastru, M. In situ characterization of preferential flow by combining plot- and point-scale infiltration experiments on a hillslope. *J. Hydrol.* **563**, 633–642 (2018).

78. Glaser, B., Jackisch, C., Hopp, L. & Klaus, J. How meaningful are plot-scale observations and simulations of preferential flow for catchment models? *Vadose Zone J.* **18**, 180146 (2019).

79. Uchida, T., Kosugi, K. & Mizuyama, T. Effects of pipeflow on hydrological process and its relation to landslide: a review of pipeflow studies in forested headwater catchments. *Hydrol. Processes* **15**, 2151–2174 (2001).

80. Wilson, G. V., Rigby, J. R., Ursic, M. & Dabney, S. M. Soil pipe flow tracer experiments: 1. connectivity and transport characteristics. *Hydrol. Processes* **30**, 1265–1279 (2016).

81. *CASTNET* (US EPA, 2019).

82. Tokunaga, T. K. et al. Deep vadose zone respiration contributions to carbon dioxide fluxes from a semiarid floodplain. *Vadose Zone J.* https://doi.org/10.2136/vzj2016.02.0014 (2016).

83. Massman, W. J. A review of the molecular diffusivities of H_2O, CO_2, CH_4, CO, O-3, SO_2, NH_3, N_2O, NO, and NO_2 in air, O_2 and N_2 near STP. *Atmos. Environ.* **32**, 1111–1127 (1998).

84. Moldrup, P. et al. Predicting the gas diffusion coefficient in repacked soil: water-induced linear reduction model. *Soil Sci. Soc. Am. J.* **64**, 1588–1594 (2000).

85. Bowling, D. R. & Massman, W. J. Persistent wind-induced enhancement of diffusive CO_2 transport in a mountain forest snowpack. *J. Geophys. Res. Biogeosci.* https://doi.org/10.1029/2011jg001722 (2011).

86. Braendholt, A., Larsen, K. S., Ibrom, A. & Pilegaard, K. Overestimation of closed-chamber soil CO_2 effluxes at low atmospheric turbulence. *Biogeosciences* **14**, 1603–1616 (2017).

87. Shi, Z. et al. The age distribution of global soil carbon inferred from radiocarbon measurements. *Nat. Geosci.* **13**, 555–55 (2020).

88. Brimhall, G. H. & Dietrich, W. E. Constitutive mass balance relations between chemical-composition, volume, density, porosity, and strain in metasomatic hydrochemical systems—results on weathering and pedogenesis. *Geochim. Cosmochim. Acta* **51**, 567–587 (1987).

Author contributions
J.W. and T.K.T. designed and conducted part of the field and laboratory work and wrote the manuscript. C.A.B., A.W.N., W.S.B. and A.N.H. conducted the field work. W.D. and M.B. conducted part of the laboratory chemical analyses. A.P.T. modelled ET. K.H.W. conducted and supervised the field work.

Competing interests
The authors declare no competing interests.

Additional information
Extended data is available for this paper at https://doi.org/10.1038/s44221-024-00293-8.

Supplementary information The online version contains supplementary material available at https://doi.org/10.1038/s44221-024-00293-8.

Correspondence and requests for materials should be addressed to Jiamin Wan or Tetsu K. Tokunaga.
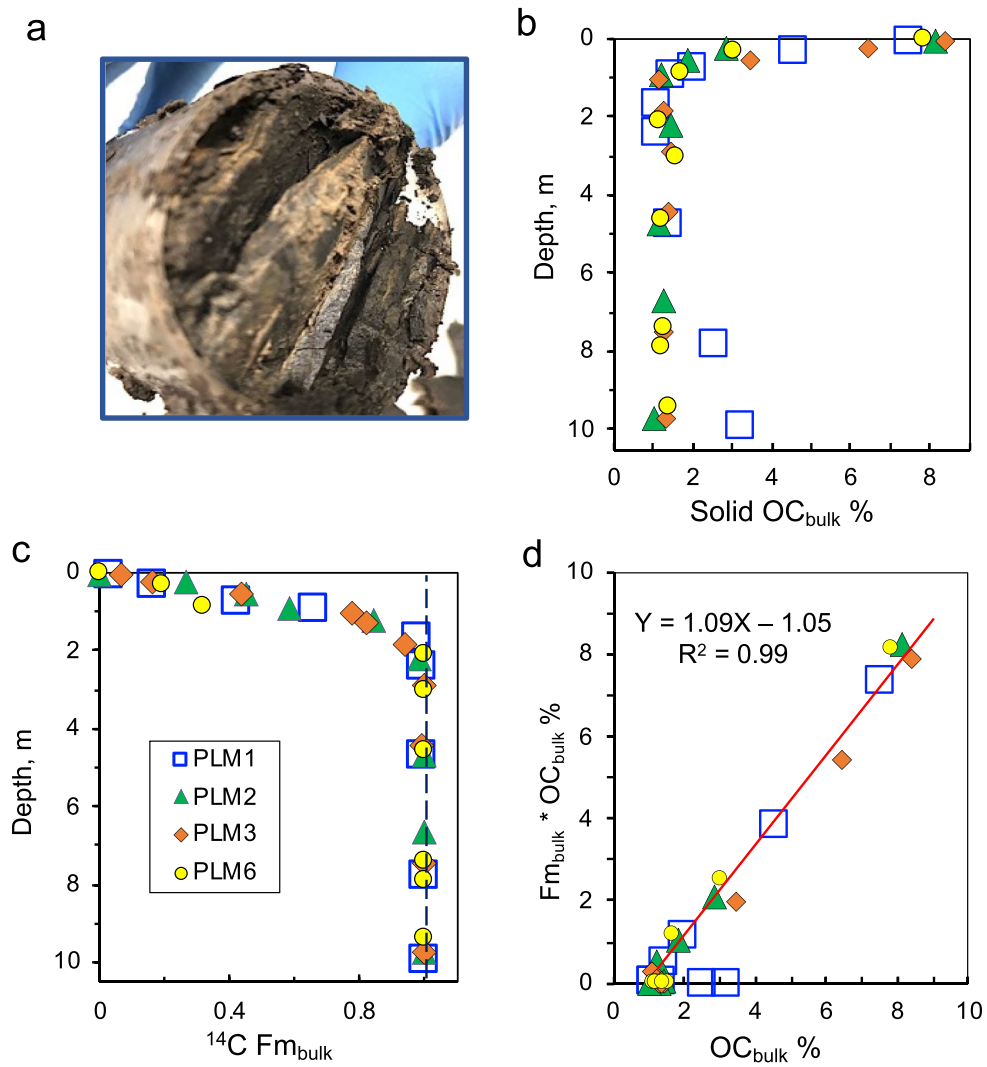
Peer review information *Nature Water* thanks the anonymous reviewers for their contribution to the peer review of this work.

Reprints and permissions information is available at www.nature.com/reprints.

Publisher's note Springer Nature remains neutral with regard to jurisdictional claims in published maps and institutional affiliations.

Extended Data Fig. 1 | Contribution of OC$_{bio}$ aging. (a) Photograph of a soil core cross section at about 1.0 m, showing rock fragments at the Soil-WZ interface. **(b)** Depth profiles of solid phase OC$_{bulk}$%. **(c)** Depth profiles of Fm$_{bulk}$. **(d)** Plots of Fm$_{bulk}$ * OC$_{bulk}$% vs. OC$_{bulk}$%.

Extended Data Table 1 | Summary of properties and processes

Inventories in Mancos Shale	method, source		
bulk density	lab-meaured core mass and dimensions	2500	kg/m^3
bedrock BC	measured (XRF)	3.86	mol$_c$/kg
bedrock S	measured (XRF, XRD)	0.570	mol/kg
bedrock S/BC	measured (XRF)	0.148	mol/mol$_c$
bedrock IC	measured (TIC)	1.214	mol/kg
bedrock OC	measured (TOC, ^{14}C)	1.272	mol/kg
bedrock IC/pyrite	measured (XRF, XRD)	4.26	mol/mol
bedrock IC/BC	measured (TIC, XRF)	0.315	mol/mol$_c$
bedrock OC/BC	measured (XRF, TOC, ^{14}C)	0.330	mol/mol$_c$
soil zone average DIC	measured	3.29	mM = mol/m^3
soil zone average DOC	measured	0.92	mM = mol/m^3
Subsurface flow and weathering			
average recharge rate	5-year water mass balance	0.175	m/yr
bedrock BC weathering rate	Darcy flow • BC conc., 5-yr. average	1420	kmol$_c$/(km^2 yr)
	standard deviation	533	kmol$_c$/(km^2 yr)
bedrock S weathering rate	Darcy flow • SO4 conc., 5-yr average	394	kmol/(km^2 yr)
	standard deviation	267	kmol/(km^2 yr)
^{14}C Fm(DIC) of efflux	flow-weighted FM(DIC efflux)	0.794	–
^{14}C Fm(DOC) of efflux	flow-weighted FM(DOC efflux)	0.811	–
global shale bedrock area	Amiotte Suchet et al., 2003, Table 5	3.42E+07	km^2

Extended Data Table 2 | Summary of C influxes

rock C influxes	method, source	kmol C (km^{-2} yr^{-1})	Mg C (km^{-2} yr^{-1})	% of total efflux
IC weathering release rate	equated to SO4 discharge rate	394	4.7	
IC weathering release rate	IC lost, based on reconstructed weathered-eroded profile	434		
IC weathering release rate	IC/BC ratio •weathering(BC)	447		
IC weathering release rate	average of SO$_4$-, BC-, and weathered profile-based methods	425	5.1	1.0%
OC weathering release rate	OC/BC ratio •weathering(BC)	468		
OC weathering release rate	OC lost, based on reconstructed weathered-eroded profile	392	4.7	1.0%
modern C influxes (soil into groundwater)				
IC influx rate	DIC(soil)•recharge rate	576	6.9	1.4%
OC influx rate	DOC(soil)•recharge rate	161	1.9	0.4%
photosynthetic rate	estimated to balance modern C cycle	39925	479	98.0%

Extended Data Table 3 | Summary of C effluxes

total (rock + modern) C effluxes	method, source	kmol C (km^{-2} yr^{-1})	Mg C (km^{-2} yr^{-1})	% of total efflux
DIC efflux	DIC•flow	644	7.7	-1.6%
DOC efflux	DOC•flow	98	1.2	-0.2%
CO$_2$ efflux	Ficks law, -D$_e$•grad CO$_2$	40000	480	-98.2%
total C exports (DIC, DOC, CO$_2$)	sum of effluxes	40742	489	-100.0%
modern C effluxes				
IC(modern) efflux	FM(DIC)•DIC•flow	511	6.1	-1.3%
OC(modern) efflux	FM(DOC)•DOC*flow	79	1.0	-0.2%
CO$_2$(modern) efflux	Ficks law - [CO$_2$(rock IC) + CO$_2$(rock OC)]	39334	472	-96.5%
rock C effluxes				
IC(rock) efflux	[1-FM(DIC)]•DIC•flow	133	1.59	-0.3%
OC(rock) efflux	[1-FM(DOC)]•DOC•flow	19	0.22	-0.05%
CO$_2$(rock IC) efflux	released IC(rock) - DIC(rock, efflux)	292	3.51	-0.7%
CO$_2$(rock OC) efflux	released OC(rock) - DOC(rock, efflux)	373	4.48	-0.9%
total rock C exported		817	9.80	-2.0%